communications earth & environment

Article

https://doi.org/10.1038/s43247-024-01249-2

Sulfide saturation and resorption modulates sulfur and metal availability during the 2014–15 Holuhraun eruption, Iceland

Check for updates

Emma J. Nicholson[1,8] ✉, Penny E. Wieser[2,8] ✉, Margaret E. Hartley[3], Frances E. Jenner[4], Barbara E. Kunz[4], Evgenia Ilyinskaya[5], Thorvaldur Thordarson[6] & Marie Edmonds[7] ✉

Mafic magmas may experience multiple stages of sulfide saturation and resorption during ascent and differentiation. Quenched tephra erupted during the 2014–15 Holuhraun eruption preserve abundant evidence for sulfide resorption, offering a rare opportunity to explore the sulfide life cycle from nucleation to resorption. Specifically, we combine detailed textural and chemical analyses of sulfides and silicate melts with geochemical models of sulfide saturation and degassing. This integrative approach demonstrates that sulfides began nucleating in melts with ~8 wt% MgO, persisted during fractionation to 6.5 wt% MgO, before resorbing heterogeneously in response to sulfur degassing. Sulfides are preserved preferentially in confined geometries within and between crystals, suggesting that kinetic effects impeded sulfur loss from the melt and maintained local sulfide saturation on eruption. The proportion of sulfides exhibiting breakdown textures increases throughout the eruption, coincident with decreasing magma discharge, indicating that sulfide resorption and degassing are kinetically limited. Sulfides likely modulate the emission of sulfur and chalcophile elements to the atmosphere and surface environment, with implications for assessing the environmental impacts and societal hazards of basaltic fissure eruptions.

The global sulfur cycle is one of the major biogeochemical cycles that regulate Earth's surface conditions and is linked directly to the long-term evolution of our planet's oxidation state and climate[1,2]. Volcanoes and their magmatic roots are important components of this cycle, transporting sulfur from the mantle into the atmosphere and oceans, controlling the recycling efficiency of sulfur at subduction zones[3–6], and sequestering sulfur in crustal cumulates or ore deposits[7–9]. Sulfur is dissolved in silicate melts as sulfide (S^{2-}) and sulfate (S^{6+} in SO_4^{2-}) species, with the proportion of each acting as a tracer of redox-sensitive processes[10–12]. Sulfur is also highly volatile and partitions strongly into magmatic fluids as SO_2, H_2S, SO_3, and S_2 species;[13–15]. The behavior of chalcophile trace elements, such as Cu, Au and Ag, in magmatic systems is intimately tied to that of sulfur, as these elements will partition preferentially into sulfur-rich exsolved fluids or immiscible sulfide melts where present[16].

Voluminous basaltic fissure eruptions (>1 km^3) such as those occuring in Iceland outgas prodigious quantities of sulfur and chalcophile elements, posing an environmental hazard that is exacerbated by relatively low plume altitudes and protracted eruption durations[17–25]. Tropospheric plumes from these predominantly effusive eruptions are time-varying mixtures of magmatic gases and particulate matter (PM), the latter includes abundant aerosols and variable quantities of silicate fragments (i.e., tephra). Aerosol PM includes condensed acidic gas species, such as sulfate, fluoride and

[1]Department of Earth Sciences, University College London, London WC1E 6BS, UK. [2]Earth and Planetary Science, UC Berkeley, Berkeley, CA, USA. [3]Department of Earth and Environmental Sciences, University of Manchester, Manchester M13 9PL, UK. [4]School of Environment, Earth and Ecosystem Sciences, The Open University, Milton Keynes MK7 6AA, UK. [5]School of Earth and Environment, University of Leeds, Leeds LS2 9JT, UK. [6]Faculty of Earth Sciences, University of Iceland, Reykjavik, Iceland. [7]Centre for the Modeling of Earthquakes and Tectonics (COMET), Department of Earth Sciences, University of Cambridge, Cambridge CB2 3EQ, UK. [8]These authors contributed equally: Emma J. Nicholson, Penny E. Wieser. ✉e-mail: emma.nicholson@ucl.ac.uk; penny_wieser@berkeley.edu; me201@cam.ac.uk

chloride, and trace metals and metalloids, such as Cu, Pb, Zn, As, Se[17,18,26–29], many of which are classified as environmental pollutants by public health agencies[17,30]. Consequently, volcanic emissions may severely degrade regional air quality[18,31] and for the largest events, impact the climate[32–35]. Acidic gases and volatile trace elements are highly soluble in water and readily dissolve in precipitation, contaminating soils and water sources and in turn, either polluting or fertilizing ecosystems[36–43].

Well-constrained volcanic sulfur budgets are critical to assessing the climatic and environmental impacts of past and present eruptions[24,25,44–47] and to predicting the outgassing flux of chalcophile metals and metalloids. Maximum dissolved sulfur concentrations in a melt are buffered by the solubility limits of S^{2-} and S^{6+}. In relatively reduced magmas where S^{2-} is prevalent (e.g., mid-ocean ridge basalts, MORB, and ocean island basalts, OIB), an immiscible Fe-Ni-Cu sulfide liquid will precipitate if the S^{2-} concentration in the melt exceeds the sulfide content at sulfide saturation ($SCSS^{2-}$, e.g.,[48–51]). If this sulfide phase is not resorbed during late-stage S degassing, it manifests as globules that range in diameter from less than one micron to several tens of microns in erupted products (e.g.,[52,53]). Importantly, saturation in an immiscible sulfide phase sequesters sulfur and chalcophile elements into the sulfide liquid, limiting the mass of sulfur and chalcophile elements available to partition into exsolved aqueous fluids[54–57]. For example, while dissolved sulfur concentrations in MORB and OIB basalts are typically on the order of 10^2 to 10^3 ppm, sulfide melt can contain in excess of ~30 wt% S. Similarly, sulfide liquid-silicate melt partition coefficients exceed 400 for elements such as Cu, Ag and Te and can be even greater for Ni and platinum group elements[54,56–58]. Therefore, even a small mass percentage of sulfide in a silicate melt will scavenge a substantial proportion of the sulfur and chalcophile element mass in the magma. Numerous studies have documented textural evidence of sulfide breakdown in the presence of an aqueous fluid phase at low pressures in magmatic-volcanic systems, which may represent a mechanism to release the chalcophile elements to the melt-vapor system on the timescale of eruption[7,47,59–64].

On cooling from magmatic temperatures, sulfide liquid fractionates an Fe-rich monosulfide solid solution (MSS), that coexists with residual sulfide melt[65–69]; chalcophile elements will partition between these two phases according to their MSS-sulfide melt partition coefficients[57,70,71]. At lower temperatures, residual sulfide melt crystallizes to Cu-rich intermediate solid solution (ISS)[65,66]. Further cooling drives the subsolidus recrystallization of MSS to pyrrhotite and pentlandite and ISS to chalcopyrite and cubanite[52,72].

Total eruptive sulfur yields into the atmosphere are often estimated petrologically based on the difference between the sulfur concentration of melt inclusions (MI) trapped in early formed crystals and degassed lavas, multiplied by erupted mass[73]. Yet, sulfide globules are commonly observed in erupted products from reduced MORB and OIB magmas[47,52,74,75]. Further, chalcophile element systematics in volcanic emissions are consistent with sulfide-melt partitioning in some cases[59,63,76]. Together, these observations suggest that sulfide saturation and, crucially, resorption of an immiscible sulfide phase, may modulate the availability of sulfur and trace elements in magmas in a way that is rarely accounted for in petrological calculations. If some S in the melt has already partitioned into a sulfide phase prior to melt inclusion entrapment, then the release of S and other trace elements back into the melt-vapor system during the resorption of these sulfides upon eruption will not be accounted for using traditional melt-inclusion derived volatile budgets. Equally, early sulfide saturation followed by fractional separation into cumulates may reduce the availability of chalcophile elements for outgassing (and ore formation) and instead sequester them in the crust[77–80]. The timing of sulfide saturation relative to the onset of fluid saturation, and the composition of that fluid, is critical to determining whether sulfur and metals are sequestered in the crust or released, either to the atmosphere or into ore-forming fluids[61,76,81–83].

Relatively reduced mafic magmas in hotspot and MORB settings may experience multiple stages of sulfide saturation and resorption in response to changes in pressure, temperature, oxidation state and melt composition during ascent and differentiation[47,48,51,61,82,84–88]. In this study, we examine sulfide globules in pyroclasts erupted during the 2014–2015 basaltic fissure eruption at Holuhraun, Iceland[53,74,89]. Among mafic eruptions from which sulfide globules are documented, pyroclasts from the 2014 to 2015 Holuhraun eruption preserve a remarkable abundance of sulfide globules, as well as diverse sulfide textures. Given the large atmospheric sulfur loadings produced during this and other basaltic fissure eruptions in Iceland, understanding the mechanisms by which immiscible sulfides nucleate, grow and resorb at low pressures in the sub-volcanic plumbing system on the timescales of individual eruptions is crucial for determining the availability of sulfur and chalcophile metals for delivery to the surface environment. We show that tephra preserve abundant evidence for sulfide resorption "caught in the act" before all available sulfide is exhausted, offering a rare opportunity to explore the processes that modulate the sulfide life cycle from nucleation through to resorption.

The 2014–2015 eruption of Holuhraun

An intense seismic swarm beginning on 16 August 2014 marked the onset of a major rifting event along a 48 km-long segment of the Bárðarbunga-Veidivotn volcanic system, Iceland, and culminated in the six-month-long effusive event at Holuhraun (29 August 2014 to 27 February 2015, with the exception of a short break in activity on 30 August 2014; Supplementary Fig. 1). Geophysical, geochemical, and petrological monitoring data were collected at high temporal and spatial resolution during this eruption, providing holistic insights into the relationships between subsurface and eruptive processes in near real-time[37,90]. The eruption at Holuhraun extruded 1.1–1.2 km^3 of basaltic lava (Dense rock equivalent, DRE;[91]), covering an area of 84 km^2, and was the largest effusive eruption in Iceland to date since the Laki eruption (1783–1784 CE). Mass eruption rates peaked at 560 m^3/s in September 2014[91], producing intense lava fountaining (occasionally >100 m in height) that diminished over the course of the eruption. Eruptive intensity had reduced to weak lava fountaining by early October 2014 and the eruption was purely effusive by late January 2015.

The Holuhraun eruption plume was sulfur-rich but halogen-poor e.g.,[92]. Average SO_2 emission rates were ~610^{+310}_{-180} kg s^{-1} (53^{+27}_{-16} kt d^{-1}) over the six months of the eruption, peaking at a daily average of ~2170^{+830}_{-770} kg s^{-1} (~187 kt d^{-1}) on 21 September 2014[92]. Emission rates were highest during the first month of the eruption and declined abruptly in early October, followed by a slower but more steady decline for the remainder of the eruption[91,92]. Although remote in location (100 km from the nearest towns), the eruption at Holuhraun caused substantial environmental pollution[18,37] and public health impacts[93,94] across Iceland. The eruption plume degraded air quality on a regional scale, exceeding hourly air quality standards for SO_2 (350 μg/m^3; European Commission) as far as Reykjavik (250 km from the eruption site), and altered the chemistry of snow and precipitation around Iceland[37,43,95]. Intermittently, gas emissions increased ground-level SO_2 and sulfate concentrations across Europe[37,96,97]. Post-eruptive degassing from the cooling lava flows continued for a further three months after extrusion ceased, but contributed <1% of the syn-eruptive SO_2 release[98]. The 2014–15 Holuhraun eruption underlined the societal relevance of sulfur and trace element emissions, especially during prolonged fissure eruptions, and consequently the need to improve our understanding of the magmatic processes that control plume abundances.

Results

Sample petrography and sulfide distribution

Fresh, glassy tephra samples were collected throughout the 2014–2015 Holuhraun eruption from locations close to the eruptive vent. We selected three samples—H14, MSR291014 (MSR) and EI220115 (EI)—representing initial, intermediate, and final eruptive phases, respectively—for the textural and compositional analyses in this study (see Supplementary Dataset 1). These samples are splits of those described and analysed by ref. 89 and ref. 99. We sieved bulk tephra samples in phi intervals (φ) and mounted lapilli from the 2 to 4 mm (−1φ) and 4–8 mm (−2φ) size fractions in carbon-coated polished grain mounts. We imaged crystal-vesicle textures and sulfide microstructures using scanning electron microscopy (SEM) and

measured the major, trace and volatile (S and Cl) element concentrations in matrix glass, sulfides, and silicate mineral phases using electron probe microanalysis (EPMA) and laser ablation inductively coupled plasma mass spectrometry (LA-ICP-MS). Full analytical details are described in the Methods and Supplementary Notes 1–2.

All samples are predominantly vesicular sideromelane, with smooth outer surfaces that are occasionally broken to expose thin quenched margins and bubbly interiors. Clasts contain macrocrysts (>1 mm long axis) of plagioclase (pl), olivine (ol) and clinopyroxene (cpx); smaller microphenocrysts (generally <0.5 mm) of all phases; and polymineralic crystal clusters (plagioclase and clinopyroxene ± olivine; Figs. 1 and 2), all within a glassy matrix. We use the term crystal cluster to avoid implying any genetic mechanism (i.e., growth vs synneusis); however, the radial morphology is similar to plagioclase growth textures reported from experimental and natural samples[100]. Many plagioclase microphenocrysts have moderately skeletal swallow-tail morphologies. Several larger crystal clusters (generally 300 to 600 µm in diameter) exhibit equant textures more similar to those of cumulates (Fig. 2d).

In addition to silicate mineral phases, we find sulfides in the form of circular (near-spherical in 3D[101]) to elliptical Fe-S-Cu-Ni globules that range from ~1 µm to 43 µm in diameter. Sulfides are distributed heterogeneously throughout clasts, but most often situated close to either microphenocrysts, crystal clusters (of varying sizes and textures) or vesicles (Figs. 1 and 2; see also Supplementary Figs. 2–5). We classify sulfides into five groups, according to their spatial associations. Sulfides situated more than 10 µm away from any crystal or vesicle (in 2D) are defined as matrix glass-hosted, although sulfides within this category are potentially in contact with phases occurring beneath the exposed surface. Crystal-adjacent and vesicle-adjacent sulfide globules are those within 10 µm of any crystal surface or vesicle wall, respectively. Within these categories, we make a distinction between those globules near to the crystal/vesicle surfaces, and those in contact with them. We refer to sulfide globules enclosed within mineral phases as sulfide inclusions, unless they are contained within pockets of trapped silicate melt (melt inclusion-hosted).

We characterized a population of 97 sulfides in one sample H14 (31 August 2014) for their spatial associations. We find that 34 sulfide globules (35%) are close to crystals, of which 27 are in physical contact with the crystal surface based on 2D intersections (e.g., Fig. 1c–d); this proportion would likely be larger if we had constraints in three dimensions. Generally, contact angles at the crystal-sulfide interface are high, ranging from 122 to 158° with a mode of 145–150° (Fig. 3). Sulfide-plagioclase and sulfide-clinopyroxene contact angles are similar; however, attachment to plagioclase is far more common. Our observations indicate that sulfide liquid wets crystal surfaces poorly but does form attachments. Twenty-six sulfides (27%) are associated with vesicles (e.g., Fig. 1e–f), of which 14 appear attached to the vesicle surface (Fig. 1g). Vesicle-sulfide contact angles span a very broad range from 58° to 180° (Fig. 3). The relative sizes of vesicles and sulfides in vesicle-sulfide aggregates also vary; although, in most cases the sulfide globule appears in contact with a vesicle considerably larger than the sulfide diameter (Fig. 1h). Twenty-two sulfides (23%) are hosted within the matrix glass with no apparent association to either bubbles or crystals, but it is acknowledged this may not be the case in 3D. Sulfides hosted within minerals either in melt inclusions or as sulfide inclusions (e.g., Fig. 1a, b), comprise only 15% of the total population.

We measured the size distribution of sulfide globules for sample H14 based on SEM mosaics of four lapilli cross-sections (see Methods). Corrected 3D size distributions show that the sulfide number distribution is strongly negative-skewed, with sulfides most abundant in the smallest size classes (Fig. 4b, from measured 2D diameters shown Fig. 4a). In contrast, the sulfide volume distribution is strongly positive-skewed and dominated by fewer, larger sulfides; ~65% of the total volume is contained within the two largest size classes, >16 µm (Fig. 4d). The total sulfide number density across all size classes is ~600 mm^{-3} and, when combined with the size distribution, translates to a volume percent of 0.07 ± 0.03 vol% sulfides (vesicle and

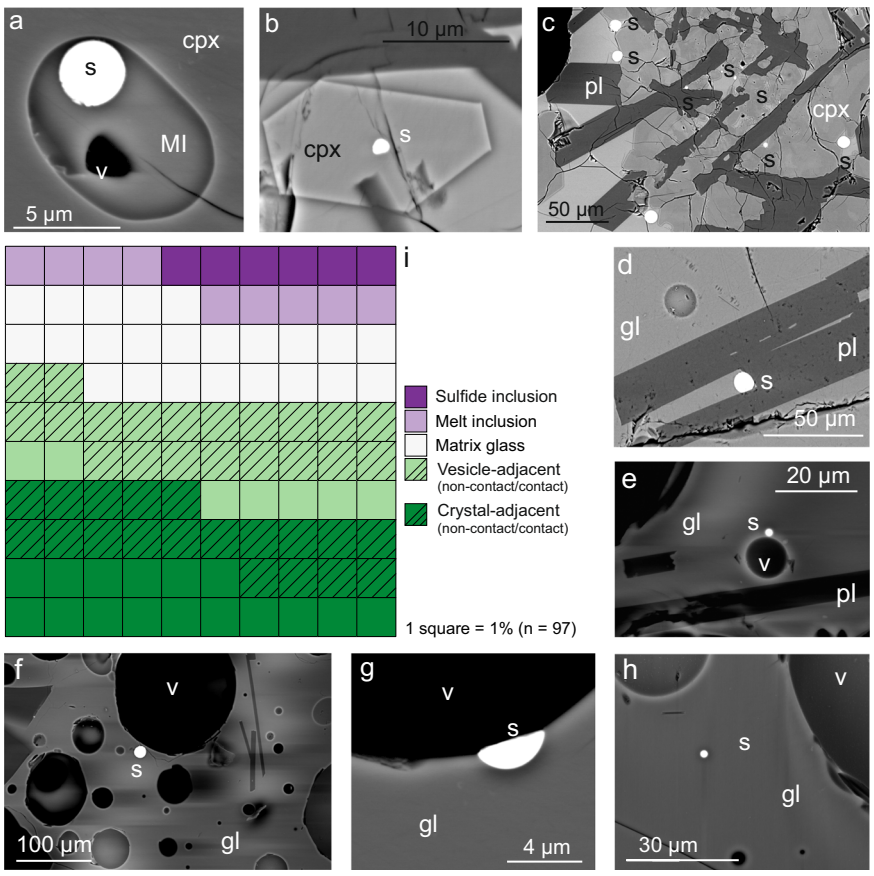

Fig. 1 | Spatial distribution of sulfides in Holuhraun tephra. a Sulfide within a melt inclusion hosted in a clinopyroxene microphenocryst. Sulfide inclusions are also present in olivine and plagioclase-hosted melt inclusions. **b** Sulfide as an inclusion within a clinopyroxene microphenocryst; similar inclusions are also present in plagioclase. **c** Sulfides near to or in contact with two- or three-phase glomerocrysts/intergrowths of plagioclase, clinopyroxene and olivine (in order of decreasing abundance). **d** Sulfide within a crystal embayment; these also occur within tight geometries between touching crystals. **e–g** Sulfides near to or in contact with vesicles. **h** Sulfides within the matrix glass. **i** The proportion of sulfides in each spatial group for sample H14 (see main text for details of classification criteria). Abbreviated annotations refer to sulfide (s), silicate glass (gl), plagioclase (pl), clinopyroxene (cpx), vesicle (v), melt inclusion (MI). Images taken from all samples.

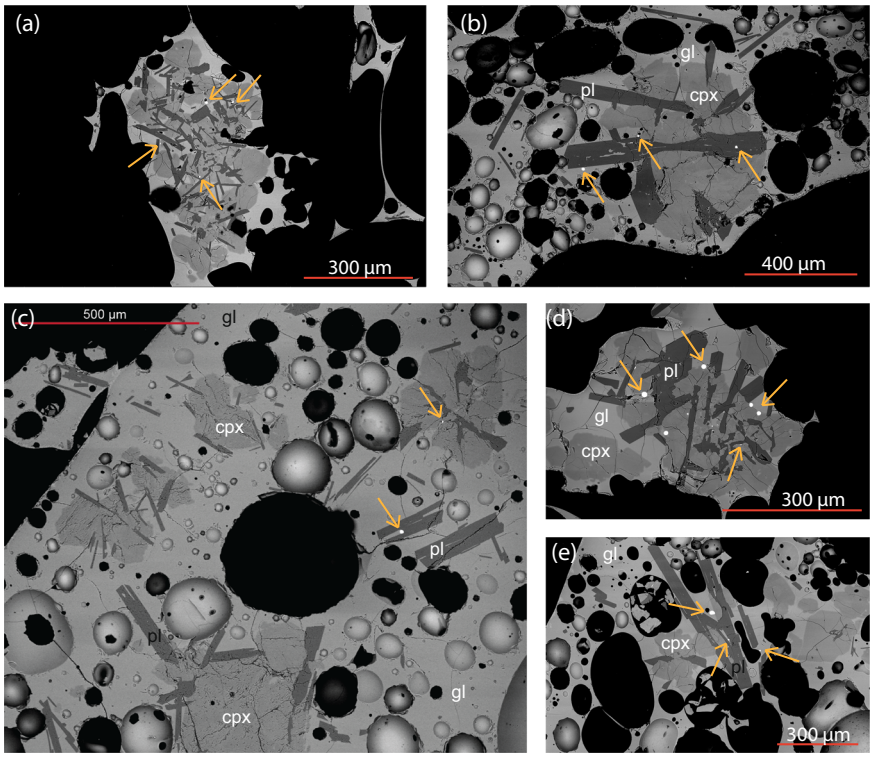

Fig. 2 | Back-scatter electron images showing sulfides within two- and three-phase glomerocrysts of plagioclase and clinopyroxene ± olivine (glomerocrysts typically between 300 and 600 µm in diameter). Sulfides are often found either attached to crystal exterior surfaces, or as inclusions in these glomerocrysts (most commonly within confined regions, see orange arrows for examples). **a**, **d** Images from sample MSR, 29 October 2014, and (**b**, **c**, **e**) images from sample H14, 31 August 2014. Abbreviated annotations refer to silicate glass (gl), plagioclase (pl), and clinopyroxene (cpx).

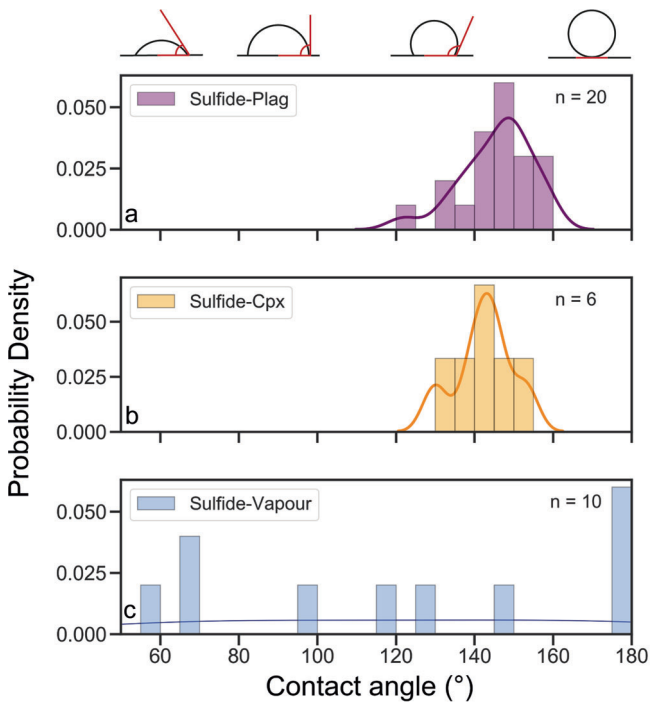

Fig. 3 | Contact angles (Θ) between sulfides and different features. a plagioclase, (**b**) Clinopyroxene, (**c**) vesicles in silicate melts. Θ < 90° indicates good wetting between the sulfide liquid and either the solid or vapor surface, whilst Θ > 90° indicates poor wetting. Θ = 180° indicates non-wetting. Data from all three samples. The curve shows the smoothed probability density function.

phenocryst-free basis). The number density, *n*, is related to the size, L, by an exponential distribution (linear trend on ln(n) vs size plot; Fig. 4c), with a slope of $-133 \pm 11\ mm^{-5}$. This slope translates to a characteristic size of ~7.5 µm (see Methods).

Sulfide textures

Sulfide globules display various exsolution textures, which we categorize into five textural types: (1) Homogeneous, (2) Fine-grained, (3) Coarse-grained, (4) Zoned, (5) Breakdown (Figs. 5 and 6). Criteria for types 2–4 follow those defined by ref. 52, to which we add two further categories to represent the broader range of textures observed in these samples. Classification is based on both textural and geochemical observations. Homogeneous sulfides have no visible compositional variation and are generally perfectly circular in 2D with smooth outlines. Fine-grained sulfides show micrometric intergrowths of Fe-Ni-rich and Cu-Fe-rich domains, representing quenched MSS and ISS respectively. Globules have highly circular cross-sections with smooth outlines. Coarse-grained sulfides also exhibit Fe-Ni-rich (MSS) and Cu-Fe-rich (ISS) intergrowths, but each of the compositional domains are much larger than in fine-grained sulfides (>0.5 µm and often several µm in size) and can be readily distinguished. The outlines of coarse-grained sulfides are generally circular, but with sub-micrometric roughness. In some globules, complete separation of Fe-Ni-rich and Cu-Fe-rich domains has taken place. This results in a zoned texture that reflects migration and subsequent crystallization of the residual Cu-rich sulfide liquid remaining after MSS crystallization[52]. A Ni-rich phase often borders the MSS-ISS interface or is present as flame-shaped structures within MSS domains. Zoned sulfide globules often exhibit crenulated outlines yet retain a circular or elliptical two-dimensional morphology. Lastly, sulfides undergoing breakdown have highly irregular morphologies with jagged outlines and hollow or honeycomb-like centers. Individual compositional domains are no longer recognizable (Fig. 5f). The remaining sulfide residue is generally Fe-rich and S-poor.

Overall, the sulfide population is dominated by Type 1 (homogeneous, Fig. 5a) and Type 2 (fine-grained, Fig. 5b) textures. In sample H14, for which the greatest number of sulfides has been classified for texture ($n = 109$), Type 1 and 2 sulfides account for 40% and 36% of the total population, respectively (Fig. 5a). Only 10% of sulfides are Types 3 and 5 (coarse-grained and breakdown, Fig. 5d, f) and 4% are Type 4 (zoned, Fig. 5e). The relative proportions of the different sulfide textures vary between the three samples analysed—that is, with time through the eruption (Fig. 5). Whilst only ~12% of sulfides were classified as Type 5 (breakdown) in H14 (31 August 2014),

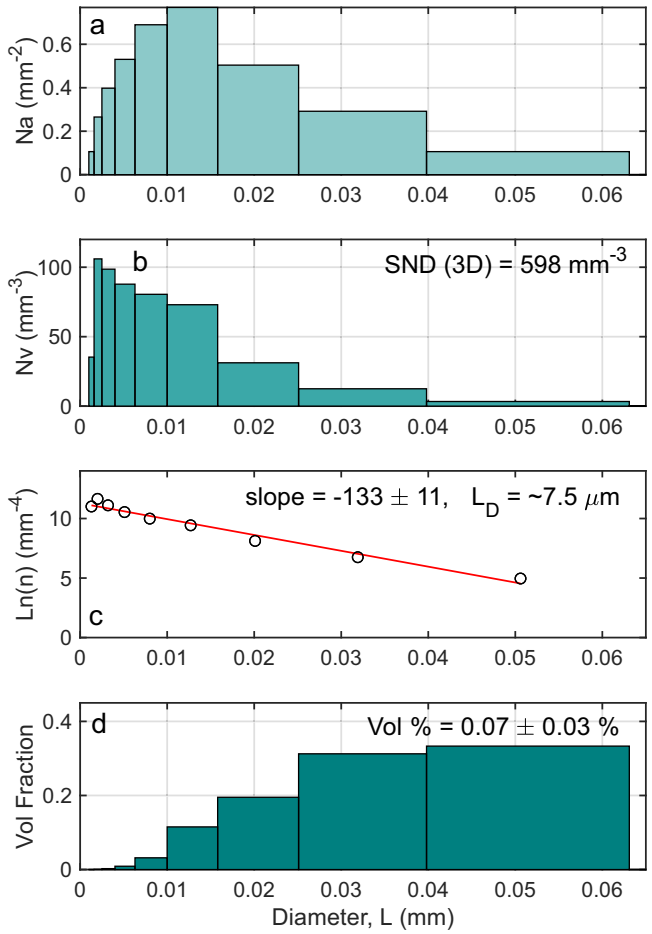

Fig. 4 | Sulfide size distributions. a Number per unit area (2D; mm^{-2}), using crystal- and bubble-free melt area; **b** Number per unit volume (3D; mm^{-3}), calculated using CSDCorrections[169]; **c** Population density (mm^{-4}), where *n* is the slope of the cumulative N_v distribution with units of number per size class per volume; the characteristic size (L_D) is calculated from −1/s where s is the slope; **d** Volume fraction, expressed as the fraction of the total sulfide volume. Data from sample H14.

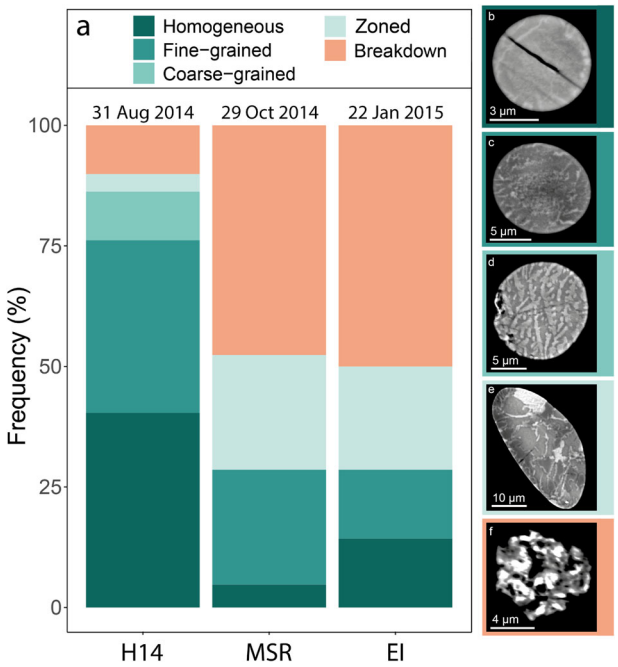

Fig. 5 | Sulfide textures through the eruption. a The proportion (%) of different sulfide textures present within each sample analysed, where time through the eruption increases from left to right; *n* = 109 (H14), 21 (MSR) and 14 (EI). See main text for description of each textural class. backscattered electron scanning electron microscope images showing sulfide globules representative of each textural class: (**b**) Type 1, Homogeneous, (**c**) Type 2, Fine-grained, (**d**) Type 3, Coarse-grained, (**e**) Type 4, Zoned, (**f**) Type 5, Breakdown. Colored borders on (**b**–**f**) correspond to the colors used in (**a**).

this proportion rose to 48% in MSR291014 (29 October 2014) and 50% in EI220115 (22 January 2015). When recalculated to exclude those sulfides breaking down, the relative proportions of Types 1–4 are similar between the three samples. Notably, coarse-grained sulfides are not recorded in the samples from the intermediate or final eruptive phases.

We find that sulfide size and texture are correlated. As the diameter of globules increases, so does the size of compositional domains (Supplementary Fig. 6). All globules less than 5 µm have a homogeneous texture, whilst all those >20 µm have a coarse-grained or zoned texture. The size distribution of zoned globules, expressed as the interquartile range in D_{eq} (see Methods), overlaps with that of coarse-grained sulfides, but extends to larger dimensions up to the maximum observed sulfide diameter of 43 µm. The size distribution of sulfides breaking down appears similar to that of fine-grained globules, although their irregular morphology (Fig. 5f, Supplementary Fig. 7) means that D_{eq} is not an intuitive measure of size and may not reflect the original diameter of the globule. Globules hosted within matrix glass or melt inclusions are generally <15 µm in diameter. The largest sulfides are always observed near or in contact with crystals (Supplementary Fig. 6).

Sulfide globules are generally circular (and assumed spherical in three dimensions) or slightly elliptical. We quantify globule shape using Form Factor (FF; Eq. 1), a shape parameter measured from binary (thresholded) SEM images. This parameter quantifies the difference between the perimeter of a sulfide globule and that of a circle of equivalent area, and is expressed on a scale from 0 to 1 (where a perfect circle = 1):

$$FF = \frac{4\pi A}{P^2} \quad (1)$$

where P refers to the 2D perimeter of the sulfide and A refers to the 2D area of the sulfide. Form Factor therefore provides an efficient single descriptor of globule 'irregularity' as it accounts for both surface roughness and elongation[102,103]. We find that the FF distribution for sulfides is heavily skewed towards high values—that is, very smooth, circular outlines—with mode of FF = 0.7–0.8 (Supplementary Fig. 4). Nevertheless, the distribution has a long tail to values as low as FF = 0.1, which reflects those sulfides in various stages of breakdown: 83% of sulfides with FF < 0.3 are classified as Type 5. FF distributions indicate, approximately, the extent of sulfide breakdown in a sample and can be easily automated.

Exploring the relationship between sulfide textures and their spatial distribution, we find that whilst homogeneous and fine-grained sulfides are found in all locations, coarse-grained and zoned globules are generally only observed adjacent to crystals (either close to or in contact with; Supplementary Fig. 6). Most sulfides hosted in melt inclusions are visibly breaking down. We note that several melt inclusions are associated with fractured crystals, which would promote decrepitation and degassing if the inclusion is intersected[104], although this cannot explain all examples. Alternatively, given the irregular and often skeletal crystal morphologies it is feasible that some melt inclusions are not isolated in three-dimensions and are instead situated within melt re-entrants. Melt inclusions may also be experiencing post-eruptive oxidative changes affecting sulfide stability[44,105]. Few Type 5 (breakdown) sulfides (<10%) are matrix glass-hosted. Importantly, these data describe how sulfides are distributed at the time of clast quenching. From textural data alone, we cannot assess the extent to which sulfide resorption has already modified the original sulfide population.

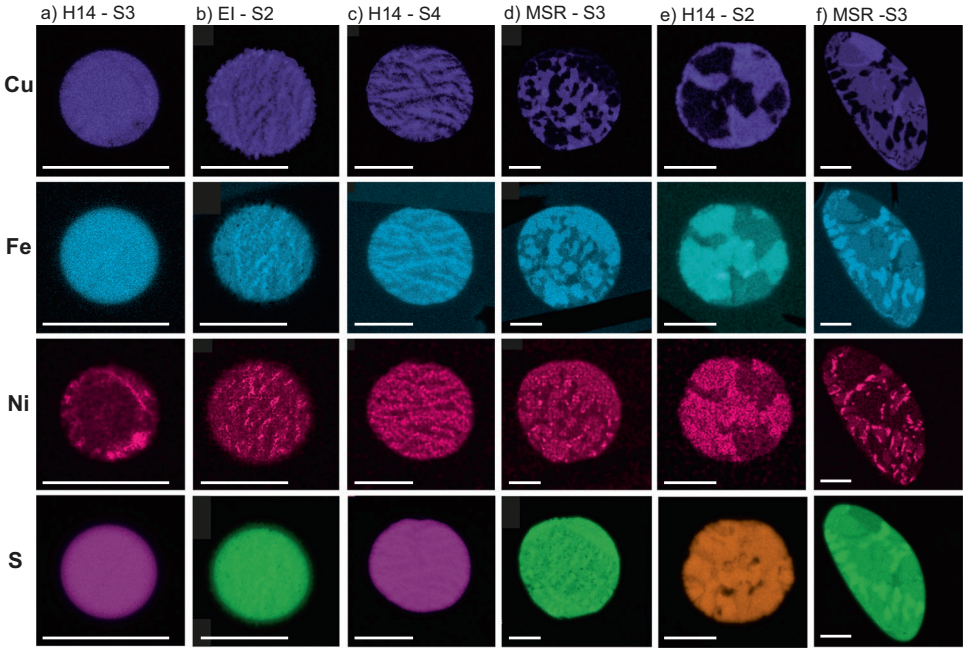

Fig. 6 | Sulfide compositions (Cu, Fe, Ni, S) from EDS mapping, showing segregation of Fe, S and Ni-rich domains and Cu-rich domains. a Homogeneous; **b** Fine-grained; (**c**, **d**) Coarse-grained; (**e**, **f**) Zoned sulfides. Labels atop each column represent sample ID and sulfide ID, corresponding to those in the supporting information. Each row is a different element. Scale bar = 10 μm in all images.

Major element sulfide compositions

Sulfide bulk compositions lie between pyrrhotite (Po) and bornite (Bnt) and overlap for sulfides erupted at different stages of the eruption (Supplementary Fig. 8). The average bulk composition based on 41 sulfides (excluding those breaking down) across all three samples is 33.6 ± 2.4 [2σ] wt% S, 46.6 ± 10.4 [2σ] wt% Fe, 2.4 ± 1.9 [2σ] wt% Ni, and 17.4 ± 11.1 [2σ] wt% Cu. Individual domains in zoned sulfides span a broader compositional range (Supplementary Fig. 8c–e), with some domains reaching Po (Fe-rich) and approaching Bnt (Cu-rich) and the Ni-rich endmember pentlandite (Ptl).

Major and trace element glass and mineral compositions

Matrix glass compositions are relatively tightly clustered in all major and selected trace elements (Supplementary Figs. 9–10) and consistent with previously published data for this eruption (6.0–6.5 wt% MgO, average 6.36 ± 0.58 wt% [2σ][53]). Clasts erupted during the final stage of the eruption have glass compositions that are slightly more evolved than those erupted at the onset of activity, with MgO contents of 6.47 ± 0.18 [2σ] wt% for sample H14 (31 Aug 2014) and 6.04 ± 0.37 [2σ] wt% for sample EI (22 Jan 2015). Sulfur contents in matrix glasses range from 394 to 1701 ppm (H14) and 333 to 1571 ppm (EI), with the highest sulfur contents found in regions of glass close to crystal clusters. Mean S contents in open glass away from crystals and vesicles are 468 ± 89 [2σ] ppm and 435 ± 125 [2σ] ppm for H14 and EI, respectively, indicating comparable amounts of S loss through degassing (~70% if we assume an undegassed melt S content of 1600 ppm). Sulfur concentrations in glass confined between crystals or interstitial within crystal clusters are substantially higher and more variable, with a mean value of 1134 ± 813 [2σ] ppm across both samples combined.

Compositional profiles measured away from sulfides show that glass sulfur concentration declines with distance from the sulfide (Fig. 7a). Sulfur concentration gradients are most pronounced for those sulfides situated in confined geometries; sulfur contents of up to 1792 ppm were measured next to sulfides, which then declined in most cases to values indistinguishable from sulfide-free matrix glass over distances of 30 to 50 μm (~455 ± 107 ppm, grey bar, Fig. 7). Profile gradients are shallower, or flat, for those sulfides situated in large regions of crystal-free glass (Fig. 7b). Although secondary fluorescence is a concern when analyses are directly adjacent to a high-concentration material, the fact that gradients are only seen away from sulfides within confined geometries and not in open regions of glass, suggests that secondary fluorescence is not contributing here. Further support that these profiles are not analytical artefacts comes from the existence of concentration gradient profiles within confined geometries without a sulfide globule present.

Average concentrations of chalcophile trace elements based on 13 analyses of matrix glasses yield 168 ± 33 [2σ] ppm Cu, 46 ± 4 [2σ] ppm Ni, 125 ± 20 [2σ] ppm Zn and 0.65 ± 0.2 [2σ] ppm Pb. Although samples are glassy and sufficiently large regions of crystal- and vesicle-free glass could easily be identified for ablation, tens of analyses were discarded due to ablation of sub-micron sulfides distributed as an emulsion throughout the matrix glass (visible as Cu and Ni spikes within the ablation signal).

Plagioclase, clinopyroxene and olivine microphenocrysts that are adjacent to sulfides, either in direct contact with or within 10 μm of sulfide globules or contain sulfide inclusions, have compositions between An = 0.62 and 0.72 (median: An = 0.7, where An = Ca/(Ca+Na+K) molar), Mg# = 0.72 and 0.82 (median: Mg# = 0.79, where Mg# = Mg/(Mg +Fe) molar) and Fo = 0.70 and 0.81 (median: Fo = 0.77, where Fo = Mg/(Mg + Fe) molar), respectively (Fig. 8). Sulfides are present as inclusions or within melt inclusions in all three mineral phases, although are not common. Mass balance indicates that sulfides were co-entrapped during melt inclusion formation; for the sulfide shown in Fig. 1a, the melt S concentration required to produce the observed sulfide globule after melt inclusion entrapment (>3000 ppm) is unrealistic given the S contents of Icelandic magmas.

Almost all plagioclase phenocrysts analysed were homogeneous in composition from core to rim; however, three were normally zoned with An-rich cores that transitioned sharply into a lower An rim (Fig. 8f, An = 0.76 to 0.72, 0.79 to 0.68 and 0.83 to 0.70). These zoned plagioclase crystals contained sulfides within melt inclusions only in the outer, more evolved, rim (Supplementary Fig. 5). Several clinopyroxenes associated with sulfides exhibited weakly developed sector zoning, with differences in Mg# of 0.02–0.03 between sectors within the same crystal (e.g., Mg# = 0.77 and 0.80 from one example in sample H14).

Discussion

We have presented textural and geochemical observations that together inform our understanding of sulfide systematics during the 2014–15 Holuhraun eruption. Sulfide globules are ubiquitous in rapidly quenched

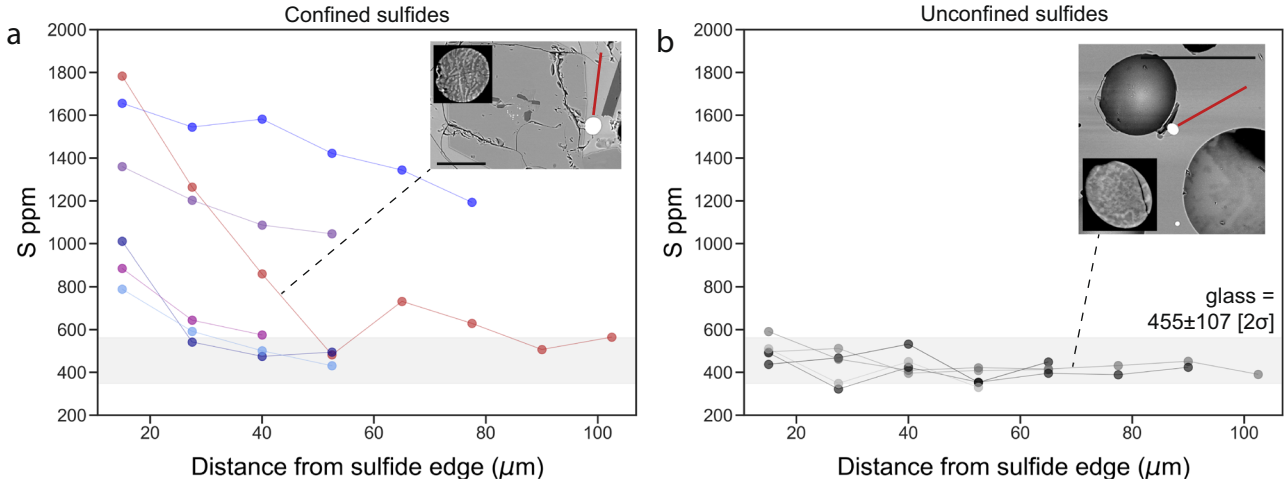

Fig. 7 | Sulfur concentration as a function of distance from sulfide globules. **a** Gradients away from sulfide globules are preserved over distances of 10–40 μm from the melt-sulfide interfaces, where sulfides are present within confined geometries within crystal clusters. **b** Similar gradients are not observed for sulfides within the matrix glass. Inset images: Backscattered electron SEM images of sulfides in Holuhraun tephra, in which the measured profile is shown by the red line: A (sample H14, scalebar is 40 μm) and B (sample H14, scalebar is 100 μm).

tephra and exhibit variations in texture and composition in both time and space that describe the complete life cycle of sulfide nucleation, growth, segregation and ultimately, resorption. Here, we discuss the processes underpinning each phase of this life cycle, model the timing of sulfide saturation relative to crystal fractionation, and evaluate the extent to which sulfide growth and resorption may modulate sulfur and chalcophile outgassing during basaltic eruptions that are sulfide-saturated at the onset of sulfur degassing.

Modeling the onset of sulfide saturation

Several different parameterizations exist for the $SCSS^{2-}$ as a function of pressure, temperature, and melt composition. However, many models were calibrated on experiments containing pure FeS liquids[85], while sulfides in the 2014–15 Holuhraun tephra contain considerable quantities of Cu and Ni (Supplementary Fig. 8). As the $SCSS^{2-}$ reduces with decreasing ratios of Fe/(Fe+Ni+Cu) in the sulfide melt (Fig. 6), models neglecting the Ni and Cu content of sulfides substantially overpredict the $SCSS^{2-}$ [47]. We use the $SCSS^{2-}$ models of Smythe et al.[51] and O'Neill[50] to predict the maximum concentration of S^{2-} that can dissolve in the melt; both models account for the ratio of Fe to Cu and Ni in the sulfide. All sulfide saturation-related calculations were performed in the open-source Python3 tool PySulfSat[106].

To assess the onset of sulfide saturation in Holuhraun lavas, we model a fractionation path reproducing the major element compositions of melt inclusions corrected for post-entrapment crystallization[89,99], whole-rock compositions[53], Holuhraun matrix glasses from ref. 53 and this study, and glasses interpreted as older Bárðarbunga deposits[107–109] using Petrolog3[110] (Supplementary Fig. 9). Interestingly, the trajectories of PEC-corrected Holuhraun melt inclusion compositions from Hartley et al.[89] and Bali et al.[99] diverge at MgO contents >9 wt%, particularly with respect to CaO, Al_2O_3 and FeO. As only Bali et al.[99] report S data from their melt inclusions, we optimize our models to fit the major element systematics of these inclusions to allow direct comparisons between the calculated $SCSS^{2-}$ and measured S contents. As the starting composition for models, we use the mean major element composition of PEC-corrected inclusions with MgO >10 wt%[99]. We use mineral-melt models for olivine, plagioclase and clinopyroxene from Langmuir et al.[111], and set the initial melt H_2O content at 0.15 wt% (following ref. 99). We note that melt water contents do not affect the phase stability fields[111], but they do slightly affect the $SCSS^{2-}$ calculated using the model of Smythe et al.[51]. We set the pressure at 3.2 kbar based on melt inclusion equilibration pressures[89] and use the Petrolog3 output temperature. Models were run assuming a closed system for O_2 with an initial $Fe^{3+}/\Sigma Fe$ ratio of 0.1. At the mean MgO content of matrix glasses analysed in this study (6.3 wt%) the $Fe^{3+}/\Sigma Fe$ ratio is 0.15. Although the oxidation state of the Holuhraun melt has not been evaluated explicitly, this modeling constraint is consistent with the range of fO_2 measured from other volcanic systems in Iceland, which suggest oxidation states relative to the FMQ buffer of −0.32 to +0.06 (Reykjanes Ridge[112]), +0.4 (Laki parental[105]), −0.4 to +0.4 (Surtsey[113]) and 0.1 ± 0.5 and 0.5 ± 0.5 (Brattaskjól and Hvammsmúli units, Eyjafjallajökull[114]).

The two $SCSS^{2-}$ models used are sensitive to sulfide composition[50,51], so this parameter must be defined at each fractionation step. While both models have in-built functions to calculate the composition of the sulfide liquid from the user-supplied melt composition, these compositions have been shown to deviate substantially from measured sulfide compositions in Hawaiian samples at high MgO contents[47]. To account for this, we ran $SCSS^{2-}$ models under two scenarios. The first assumes that the Fe/(Fe+Ni+Cu) ratio of sulfides is equal to the mean measured bulk sulfide composition (Fe/(Fe+Ni+Cu) = 0.7118) and remains constant throughout the fractionation interval. The second scenario uses the calculated sulfide compositions from each model, based on a specified liquid line of descent for Cu and Ni produced in Petrolog3[110]. We modeled Ni concentrations using initial Ni contents of 220 ppm, $K_{D,Ni}^{Ol/Melt}$ using the model of ref. 115, $K_{D,Ni}^{Clinopyroxene/Melt} = 2.6$[116] and $K_{D,Ni}^{Plag/Melt} = 0$. We modeled Cu concentrations using initial Cu contents of 80 ppm, $K_{D,Cu}^{Ol/Melt} = 0.1$, $K_{D,Cu}^{Clinopyroxene/Melt} = 0.21$ and $K_{D,Cu}^{Plag/Melt} = 0.14$[117,118]. These Petrolog3 models approximate the liquid line of descent defined by LA-ICPMS glass measurements (this study) and whole-rock measurements[53] from the 2014–15 Holuhraun eruption, as well as glass measurements from older Bárðarbunga deposits[107] (Supplementary Fig. 9). Ideally, the Fe, Ni and Cu concentrations in the melt would be adjusted iteratively based on the calculated amount of sulfide formed in each step. However, there is insufficient published Ni and Cu data to ground-truth such an iterative approach, and our models effectively recreate observed Ni and Cu concentrations (as measured by ICP-MS) that define fractionation trends.

The $SCSS^{2-}$ models predict the onset of sulfide saturation at the point of intersection between the modeled $SCSS^{2-}$ paths and a fractionation trajectory for sulfur assuming no sulfide formation (e.g., incompatible behavior, assuming initial melt S concentration was 790 ppm; Fig. 9a, b, black lines). For fixed and calculated sulfide compositions, the $SCSS^{2-}$ values from both models[50,51] are remarkably similar, predicting sulfide saturation at ~8 and ~8.6 wt% MgO respectively (Fig. 9a, b). Importantly, both models capture the prominent kink in the trajectory of melt sulfur content defined by melt inclusions, resulting from sulfur initially behaving incompatibly during sulfide-undersaturated fractionation and then following the trajectory of the

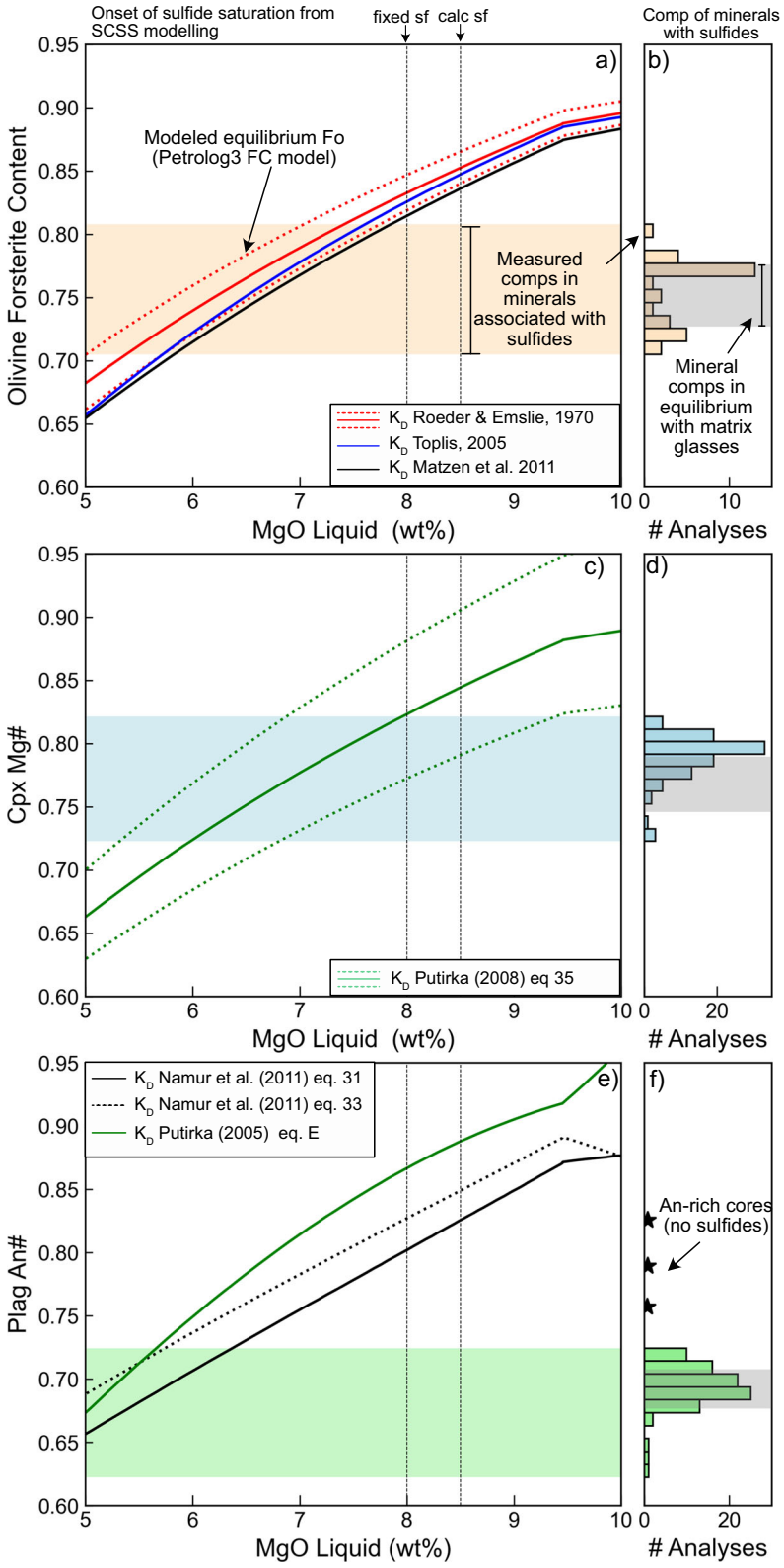

Fig. 8 | Mineral equilibrium compositions during fractional crystallization vs. appearance of sulfides in contact with or within 10 µm of each phase. Colored lines on (**a**, **c**, **e**) show equilibrium mineral compositions calculated from the liquid composition outputted by the Petrolog3 fractional crystallization model. Histograms (**b**, **d**, **f**) show measured mineral compositions either in contact with or within 10 µm of sulfide globules- the range of these histograms are indicated as shaded colored regions in (**a**), (**c**), and (**f**). Gray regions on (**b**, **d**, **f**) show mineral compositions in equilibrium with matrix glasses. Vertical gray lines on (**a**, **c**, **e**) indicate the onset of sulfide saturation from SCSS modeling (see Fig. 9 and main text) between 8 wt% MgO (fixed sulfide composition) and 8.6 wt% MgO (model calculated sulfide composition. Olivine equilibrium contents in (**a**) calculated using the K_d model of ref. 171 (0.3 ± 0.03, red line and dashes), model of ref. 172 (K_d = 0.34, black line) and the melt-composition and temperature sensitive model of ref. 173 (blue line). The gray shaded regions in (**b**) use K_d = 0.3 (ref. 172). (**c**–**d**) Calculated clinopyroxene (cpx) contents in equilibrium with melts from the Petrolog3 model calculated using Eqn. 35 from ref. 174 (± 0.08 error). **e** Calculated anorthite (An) contents in plagioclase in equilibrium with melts from the Petrolog3 model, using the anhydrous thermodynamic model of ref. 175 (solid black line), the non-thermodynamic basaltic model of ref. 175 (dashed black line) and eqn. E of ref. 176 (green line). **f** Gray shaded regions use ref. 175. The compositions of An-rich plagioclase cores are shown by the black crosses; these three crystals contain sulfides as inclusions only in the outer, more An-poor rim.

$SCSS^{2-}$ after the onset of sulfide saturation. The two models effectively bracket the most S-rich melt inclusions for <8 wt% MgO.

Calculated sulfide compositions yield $SCSS^{2-}$ values that are slightly lower at high MgO contents than the fixed composition models (because at high MgO the predicted Fe/(Fe+Ni+Cu) ratio in the sulfide is lower than measured here). At <8 wt% MgO, the models are very similar, and the calculated sulfide composition lies within 1σ of the measured sulfide composition (Fig. 9d).

Icelandic melts likely contain a non-negligible proportion of S^{6+} species, based on the redox state of Icelandic magmas (e.g.,[105,119]) and EPMA measurements of the S Kα wavelength shift in Icelandic glasses[120]. As $SCSS^{2-}$ models only account for the solubility of S^{2-}, while EPMA measurements of S in melt inclusions measure the concentration of both S^{2-} and S^{6+} species, the $SCSS^{2-}$ must be scaled up according to Eq. 2[121] before direct comparisons can be made. For only 10% S^{6+}, the model of Smythe et al.[51] effectively brackets the upper limit of measured S contents and predicts the onset of

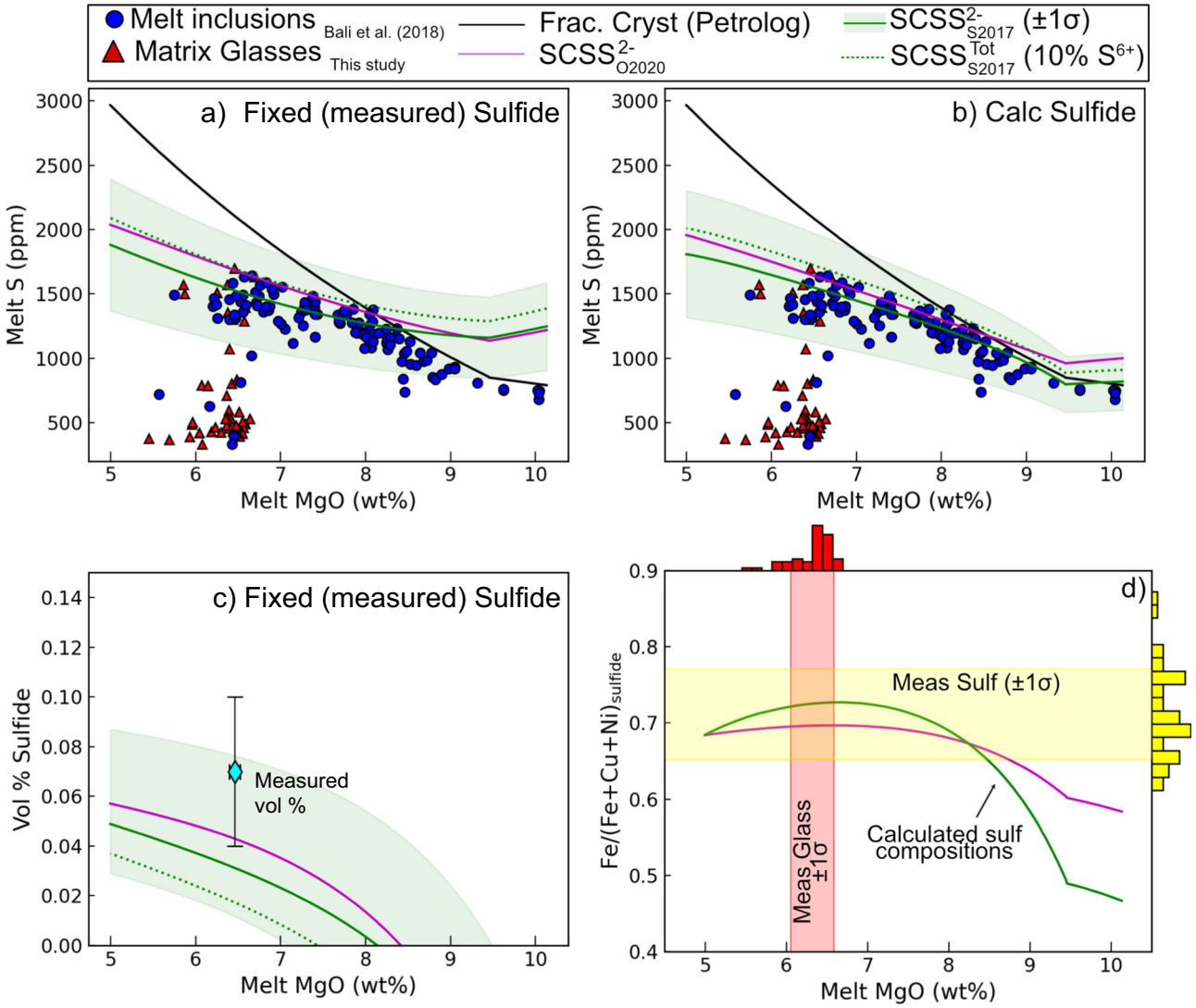

Fig. 9 | Sulfide Content at Sulfide Saturation ($SCSS^{2-}$) for different model scenarios. a Models using the mean measured bulk sulfide composition from this study. **b** Models using sulfide compositions calculated from the SCSS model. Melt inclusion compositions (blue circles) are overlain from Bali et al.[99], and glass compositions (red triangles) from this study. The expected trend in S contents for fractional crystallization without sulfide formation is shown as a black line (calculated from Petrolog3 outputs). **c** Change in volume fraction (%) sulfide as a function of melt MgO content using fixed sulfide composition. The volume percent sulfide calculated in this study is shown for comparison (light blue diamond). **d** Modeled sulfide composition as a function of melt MgO content. Measured sulfide compositions are shown for comparison and show good agreement with modeled values at the observed matrix glass composition. SCSS is modeled using the models of[51], both with and without correction for 10% S^{6+} and with no correction (just S^{2-}) using ref. 50.

sulfide saturation at very similar MgO contents to that of O'Neill[50].

$$SCSS_T = \frac{SCSS^{2-}}{\left(1 - \frac{S^{6+}}{\sum S}\right)} \quad (2)$$

We calculate the mass proportion of sulfide (X_{sulf}) formed using a mass balance:

$$X_{sulf} = \frac{S_{init} - X_{melt} S_{SCSS}}{S_{sulf}} \quad (3)$$

Where S_{init} is the initial amount of S at the start of the fractional crystallization model (790 ppm), X_{melt} is the amount of melt left during FC from Petrolog3[110], S_{SCSS} is the calculated amount of S in a sulfide saturated melt, and S_{sulf} is the average bulk sulfur concentration of sulfides (33.6 wt%). We convert this mass fraction into a volume fraction by multiplying by the density ratio of silicate melt (2804 kg m^{-3} calculated in DensityX[122]) and sulfide melt (4200 kg m^{-3},[89]). In sample H14, collected early in the eruption and exhibiting the least amount of sulfide breakdown, we measure 0.07 ± 0.03 vol% sulfide (vesicle-free basis; Fig. 4d), which lies within the 1σ uncertainty bound predicted by $SCSS^{2-}$ models at ~6.5 wt% MgO assuming a fixed sulfide composition (Fig. 9c).

Sulfides erupted in the 2014–2015 Holuhraun event are enriched in Cu compared to reported sulfide compositions from other MORB or OIB settings and are consistent with relatively late-stage sulfide saturation after substantial olivine fractionation[53,123]. Observations of sulfides as both olivine inclusions and within MIs in olivine (Fig. 1) suggest that sulfide saturation was coincident with olivine crystallization. Ni is compatible in olivine, while Cu is incompatible, so olivine fractionation drives a melt to higher Cu and lower Ni values. Additionally, the sulfide-melt partition coefficients for Cu and Ni exhibit opposing behavior as a function of melt MgO content[54]; D_{Ni} decreases sharply as MgO drops in the melt, while D_{Cu} increases slightly. Together, these effects mean that the bulk composition of sulfides will evolve towards more Cu-rich end members as crystallization progresses, reaching ~17 wt% Cu when the melt reaches <6.5 wt% MgO (Supplementary Fig. 11).

Previous studies on Icelandic melts have proposed that sulfide saturation was reached in the melt at ~6.5 wt% MgO, based on melt inclusion data from the 2000 Hekla eruption[124] and the 2014–15 Holuhraun eruption that is the subject of this study[99]. In contrast, our modeling and the prominent change in gradient in melt inclusion S contents with decreasing MgO (Fig. 9a) suggest that the Holuhraun melt reached sulfide saturation at a much earlier stage of fractionation, between 8 and 8.6 wt% MgO. The discrepancies in the timing of saturation may be a consequence of previous $SCSS^{2-}$ models assuming equilibrium with pure FeS sulfides, which tends to overpredict the $SCSS^{2-}$ compared to models incorporating Cu-Ni-rich sulfides. Overprediction of the $SCSS^{2-}$ results in a greater degree of melt fractionation prior to sulfide saturation.

In contrast, sulfur and chalcophile trace element systematics at Kīlauea, Hawai'i suggest that sulfide saturation takes place at ~12 wt% MgO, after only minor crystal fractionation[47]. The lower MgO of the onset of sulfide saturation in Iceland relative to Kīlauea likely reflects the fact that plagioclase and clinopyroxene saturate at ~9 wt% MgO in Iceland (based on Petrolog3 models; see also[125]) compared to ~6.8 wt% MgO at Kīlauea[126]. During olivine-only saturation (~10 wt% MgO), the $SCSS^{2-}$ declines towards the S fractional crystallization trajectory (Fig. 9a). In contrast, once plagioclase appears on the liquidus (at ~9 wt% MgO), an increase in melt FeO content drives the $SCSS^{2-}$ up, pushing the melt further away from sulfide saturation. Even once sulfide saturates, the near-parallel trajectories of the fractional crystallization and $SCSS^{2-}$ models means that only a small amount of sulfide is produced per unit of MgO decrease, with abundant sulfides only forming at ~6–7 wt% MgO (Fig. 9c). Differences in the onset of sulfide saturation may also reflect differences in the major element contents of primary magmas at Iceland and Hawai'i that result from their distinct mantle sources, which affects not only SCSS trajectories during fractionation but also the amount of S in primary magmas. For example, at 10 wt% MgO, Kīlauean basalts have 1200–1600 ppm S[44,47], while Holuhraun magmas have only ~800 ppm S[99] (Fig. 9).

Crystal-sulfide systematics as an independent constraint on sulfide saturation

Using the fractional crystallization model described above, we calculate the equilibrium mineral compositions for olivine, clinopyroxene and plagioclase with changing melt MgO content, for a range of the latest liquid-melt equilibration parameterizations implemented in the Python3 package Thermobar[127] (Fig. 8). We compare these equilibrium curves to the mineral compositions of crystals associated with sulfides (either as inclusions or in contact with), with a particular focus on predicted mineral compositions at the onset of sulfide saturation from $SCSS^{2-}$ modeling (8 to 8.6 wt% MgO using fixed and calculated sulfide compositions, respectively; Fig. 9).

The composition of the most primitive measured phenocrysts that host sulfides are predicted to have appeared on the liquidus at ~8 ± 1 wt% MgO (clinopyroxene) and between 7 and 8 wt% (olivine), consistent with modeled melt compositions at the onset of sulfide saturation or shortly after (Fig. 8). The remaining clinopyroxene and olivine population associated with sulfides then record a broad crystallization interval as the melt continues to evolve to ~6 wt% MgO, overlapping with matrix glass compositions.

Plagioclase crystals associated with sulfides are relatively evolved and are in equilibrium with liquids containing <6.5 wt% MgO (Fig. 8), almost entirely within the range of mineral compositions in equilibrium with matrix glass compositions. Core compositions for zoned phenocrysts indicate that plagioclase crystallization began earlier at 7–8.5 wt% MgO, coincident with that of clinopyroxene and olivine; however, sulfide inclusions are only present within the more An-poor outer rim. The often-skeletal morphologies and radial growth textures of plagioclase, particularly within smaller crystal clusters, indicate relatively rapid growth under conditions of strong undercooling[100].

These mineral-sulfide associations describe a protracted interval of melt evolution where sulfides were present in the melt either coincident with, or subsequent to, the growth of clinopyroxene, plagioclase and olivine. Hartley et al.[89] show using olivine-plagioclase-augite-melt (OPAM) barometry that while the carrier melt equilibrated at pressures of 2.1 ± 0.7 kbar, the melt inclusion population equilibrated at higher pressures centered on ~3.2 kbar corresponding to mid-crustal depths (full range 0.8 to 8 kbar). The pressure interval for carrier melt equilibration translates to depths of 7.5 ± 2.5 km, which overlaps with earthquake locations inferred to represent the dike path (6 ± 1 km[128]). We suggest that the polymineralic (plag-cpx±ol) crystal clusters (Fig. 2a–e)—many of which display core compositions more primitive than expected for the carrier liquid—represent disaggregated and entrained fragments of a relatively evolved crystal mush accumulated within a crustal storage region[129,130]. Smaller, isolated sulfide-hosting microphenocrysts may have crystallized during transport through the shallow magmatic system and during final melt equilibration. The relatively evolved mineral compositions associated with sulfides (Fig. 8), and the lack of sulfides within the most primitive cores of zoned macrocrysts, argue against very early sulfide saturation and accumulation in deep crustal cumulates, in agreement with reported temporal evolution in the crystal cargos[129]. While crystals and melts from deep, lower crustal storage zones ~17 km depth were sampled frequently by eruptions of the Bárðarbunga-Veiðivötn system in the early Holocene, petrological signatures showing upward transfer of these cargos have been largely absent in more recently erupted products[129]. Instead, since the middle-Holocene, magmas erupted in the Bárðarbunga-Veiðivötn system have mainly carried evolved macrocrysts derived from the mid-crust (7–13 km[129]). Mineral textures and compositions, combined with $SCSS^{2-}$ modeling, suggest that the final phase of sulfide saturation prior to the 2014–15 Holuhraun eruption was reached during melt differentiation within upper magmatic storage regions in the mid-crust, and persisted throughout dike transport until the onset of volatile saturation and pervasive degassing during magma ascent through the upper few hundred meters of the crust.

Sulfide nucleation and transport

The exponential sulfide size distribution (Fig. 4; similar to crystal size distributions in magmas; e.g.,[131,132]) is commonly linked conceptually with a Poisson point process, where independent events occur continuously at a constant average rate but where the exact timing of each event is random. The exponential sulfide number density in our samples (Fig. 4) suggests that once the melt reaches sulfide saturation, nucleation proceeds stochastically as a continuous, random process at a relatively constant rate. Here we are assuming that sulfide breakdown is independent of size and therefore does not bias the final distribution we observe in quenched samples. Although we cannot comment on the size of sulfides already fully resorbed, sulfides observed in partial breakdown are generally between 5 and 15 μm (Supplementary Fig. 6). If smaller sulfides were to resorb more efficiently, then the slope of our number density distribution is a minimum and thus the characteristic size may be smaller than our data suggest; further experimental studies would be needed to explore this.

Our observations indicate that sulfides commonly wet mafic crystal phases (particularly plagioclase), albeit at relatively high contact angles (Figs. 1 and 3; Supplementary Fig. 3). Previous experimental and theoretical work has suggested that magnetite and sulfide may be most important for heterogeneous nucleation of fluid bubbles that may cause flotation[7,62,133–136]. Our observations raise the intriguing possibility that silicate crystal attachment may provide an effective transport mechanism for sulfide liquid droplets—at least within the shallow magmatic system. Sessile droplet experiments involving Fe-Cu-Ni sulfide melt on an alumina substrate yield sulfide-oxide contact angles of $\Theta = 150–180°$ (compared to 122–158° in our natural samples; Fig. 3) and suggest that heterogenous nucleation of sulfides on silicate minerals is thermodynamically unfavorable due to high interfacial energies[136]. We would argue that, although wetting crystals at high angles, the widespread association between sulfide globules and crystal surfaces in natural samples cannot be by chance. Constraining the extent to which sulfide-mineral wetting behavior varies over a range of mineral and sulfide compositions will be crucial to understanding the role of crystals in both scavenging and transporting sulfides.

Flotation of sulfides in the form of bubble-sulfide aggregates has been proposed to explain how sulfides that would otherwise settle into cumulates due to their large density contrast with silicate melt may be transported into the shallow magmatic system[62,137], similar to the mechanism proposed for the flotation of magnetite[133–135]. We observe several sulfides attached to vesicles, with a wide range of wetting angles, which may represent preserved bubble-sulfide aggregates. However, direct contact with an exsolved vapor phase would promote sulfide dissolution (Supplementary Fig. 7) and we may expect that only a fraction of the original sulfide-bubble aggregates would be preserved.

Sulfide resorption

Our data and modeling suggest that sulfide nucleation in the 2014–15 Holuhraun melt began at ~8 wt% MgO and continued until the onset of sulfur degassing at ~6.5 wt% MgO, evidenced by an abrupt decrease in melt sulfur contents at constant MgO observed in matrix glasses (Fig. 9a). Partitioning of dissolved sulfur from the melt into an exsolved vapor phase would drive the melt rapidly towards sulfide undersaturation. Degassing-induced reduction of the melt[138] will counteract this effect slightly by decreasing the total solubility of sulfur as S^{6+} reduces to S^{2-}, but this relatively small effect is overwhelmed by the much larger amount of S lost to the vapor (particularly in relatively S^{6+}-poor Icelandic magmas).

The most striking observation from a textural perspective is the change in the proportion of sulfides visibly breaking down throughout the eruption, specifically between samples collected at the eruption onset (August 2014), where <10% of visible sulfides exhibited breakdown textures, compared to later samples (November 2014 and January 2015) where ~50% of visible sulfides were texturally unstable. Given that the magma effusion rate decreased throughout the eruption (i.e., from a peak effusion rate of 560 m^3/s in September 2014 to <50 m^3/s after the first three months of the eruption[91,139]), we suggest that the later erupted samples spent longer at shallow depths or in surface lava ponds after S degassing had begun, so there was additional time for sulfides to break down in response to changing melt conditions. Given that all samples likely followed similar degassing paths, this observation indicates that sulfide breakdown is kinetically-limited.

Sulfides appear to break down to a Fe-rich (S-poor) remnant[57] (Supplementary Fig. 7). Sulfide liquid reacts according to Eq. 4[59] in response to changes in either fO_2 or fS_2 to form magnetite (Fe_2O_3), which has a much lower capacity to accommodate sulfur and metals within its structure[61].

$$3FeS_{(SL)} + 2H_2O_{(melt,fluid)} + 2O_{2(melt,fluid)} \rightarrow Fe_3O_4 + 2H_2S_{(fluid)} + SO_{2(fluid)} \quad (4)$$

Sulfide exsolution textures are a size-dependent process controlled by a balance between the amount of undercooling and the time between MSS and ISS crystallization ([52], see also Supplementary Note 3). Chalcophile elements are therefore segregated, to varying degrees, during cooling from magmatic temperatures (Fig. 6) according to their relative affinity for ISS with respect to MSS, concentrating Zn, As, Cd, Sn, Sb, Ag, Te, Au, Pb and Bi in the Cu-rich ISS domains[57]. In contrast, Ni, Co and Re are retained in the Fe-rich MSS domains. A compelling question for future work is whether the metals sequestered in sulfides are released congruently during resorption. Some fractionation is possible if Cu-rich and Fe-rich domains break down through different mechanisms that are not necessarily synchronous, which may lead to a change in gas and aerosol plume chemistry.

Sulfide globules are commonly found within confined melt regions near to or in contact with crystals; such locations include skeletal embayments within individual crystals or between two radiating crystals within crystal clusters (Fig. 1). This relationship implies either preferential nucleation in these locations or preferential preservation. Sulfur is incompatible in growing silicate mineral phases and so we may expect an enriched boundary layer to form immediately alongside the crystal boundary, where elevated melt S contents may induce local sulfide saturation in close proximity to crystals growing in equilibrium with the melt. However, the presence of sulfide globules distributed throughout the samples—particularly within the open regions of matrix glass—argue against such local saturation effects. Instead, we propose that kinetic effects related to slow sulfur diffusion maintain locally elevated sulfur concentrations under disequilibrium and promote the preservation of sulfide within confined geometries. Similar processes were invoked to explain the elevated sulfur contents measured in near-vent quenched matrix glasses erupted at Fissure 8 during the 2018 Kīlauea eruption, which are elevated above those predicted by degassing models at atmospheric pressure[44].

Timescales of degassing and sulfide breakdown

Sulfur contents in glass adjacent to confined sulfide globules are elevated (800 to 1800 ppm S; Fig. 7) relative to the mean matrix glass (455 ± 107 [2σ] ppm S; Fig. 7) and in many cases overlap with those of melt inclusions at the same MgO content (1300 to 1700 ppm S; Fig. 9a). Profiles away from confined sulfides, towards open matrix glass, show a gradual decrease in melt S content until reaching values within error of the matrix composition over distances of 40 to 100 μm. The diffusivity of sulfur (D_s) in an anhydrous basaltic melt at 1170 °C and 0.1–0.5 wt% H_2O is $1.3–1.6 \times 10^{-12}$ $m^2 s^{-1}$ (Eqn. 5[140]).

$$\ln D_s = -8.21 - (27692 - 651.6C_{H2O})/T \quad (5)$$

where D_s is in $m^2 s^{-1}$ and T is in Kelvin (1170 °C + 273.15[53]), and C_{H2O} is the water content in wt%[99]. This relation is based on experimental data[141] obtained between 1250 and 1400 °C at FMQ −3 and therefore requires some extrapolation to the eruption temperature calculated based on glass compositions[53]. Calculated S diffusion rates using Eq. 5 are orders of magnitude lower than H_2O and CO_2 under similar conditions. Sulfur diffusivity (i.e., element mobility in response to a concentration gradient) will increase with both increasing water content and fO_2[140]. If sulfur loss is impeded by kinetic diffusive effects then this may delay sulfide undersaturation, such that sulfide liquid remains in equilibrium with the melt composition until eruption and quenching. If we approximate 1-D diffusion by:

$$t \approx \frac{x^2}{4D_s} \quad (6)$$

and set D_s equal to 10^{-12} and 10^{-13} $m^2 s^{-1}$, this yields an approximate timescale, t, for sulfur to diffuse over a distance (x) of 100 μm of 0.7–7 h respectively. Timescales of ascent based on dehydration of melt inclusions have been estimated as 0.48–19.2 h from olivine-hosted inclusions, and 0.48–600 h from plagioclase-hosted melt inclusions[89]. To explore potential degassing paths which can account for observed S concentration gradients in the framework of these timescales, we model dissolved volatile contents and exsolved fluid proportions using Sulfur_X[142] (see Supplementary Note 4 for degassing model parameters). We use the average composition of matrix glass from H14, assuming an initial H_2O content of 0.5 wt%, 1640 ppm CO_2, 1700 ppm S[99], a model temperature of 1150 °C. The model initiates at ~370 MPa (the pressure of vapor saturation). By the time the magma has decompressed to 100 MPa, ~74% of the total CO_2, 1–2% of the total S and ~0.24% of the total H_2O has degassed (Supplementary Fig. 12). By 10 MPa, ~98% of the total CO_2, 8–19% of the total S, and 5–6% of the total H_2O has been lost. These models demonstrate that S degasses slightly before H_2O, although by the time >10% of each gas species has degassed, the trajectories are very similar. Thus, our inferred timescales of 0.7–7 h to account for preservation of sulfur gradients spanning ~100 μm in matrix glasses (Fig. 7) and the presence of intact sulfides within degassing matrix glasses are consistent with the timescales of 0.48–600 h for loss of H_2O.

Elevated sulfur contents in matrix glasses from hydromagmatic eruptions involving shallow magma-water interaction with surface or groundwater, in both Iceland and Kīlauea, further underline how sulfur is largely retained in the melt until low pressures, as a consequence of relatively late stage degassing relative to CO_2, and slower diffusion rates relative to H_2O[23,24,45,75,107,120,143,144].

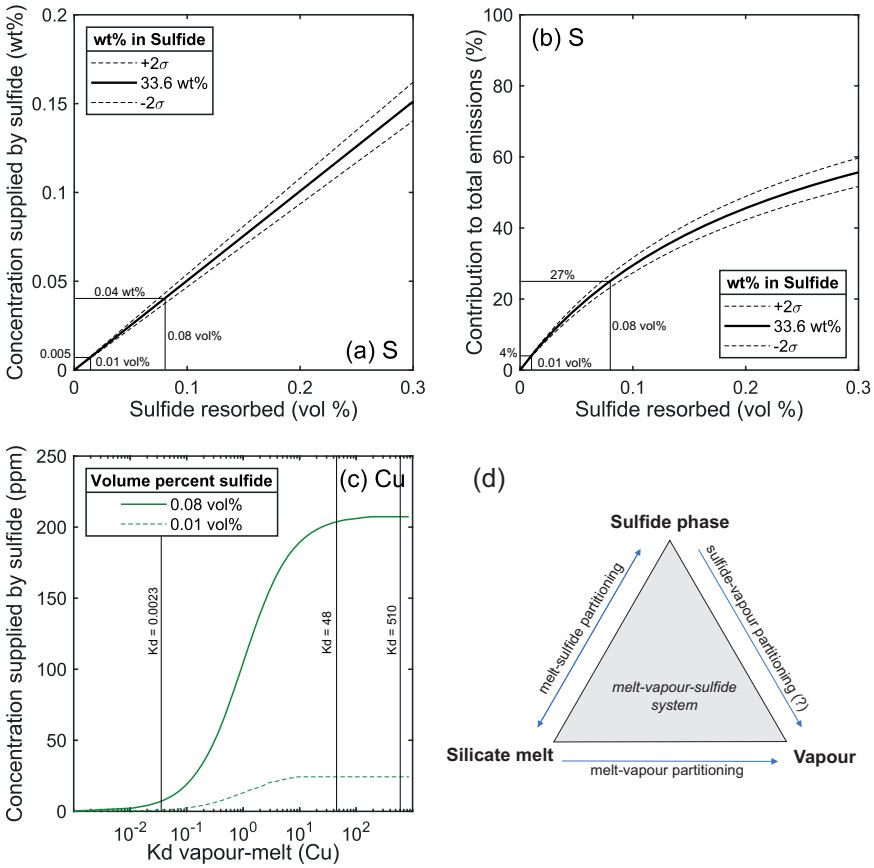

Fig. 10 | Elemental partitioning between sulfides and vapor. a Calculation of the amount of sulfur from the system released into the fluid phase (i.e., the gas plume) as a result of sulfide resorption (assuming S is highly volatile). For example, resorption of 0.08 vol% sulfide is equivalent to degassing an extra 0.04 wt% (400 ppm) S from the melt phase, The upper and lower bounds in modeled sulfide vol% (0.02 to 0.08 vol%; from Fig. 9c) are annotated to illustrate the potential contribution from resorption of the entire sulfide population. **b** Contribution of sulfide resorption as a percentage of total sulfur outgassing (degassing of initial dissolved S content in melt plus S added through sulfide resorption). Uncertainties (dashed lines) refer to ±2σ on the measured sulfide bulk composition. See main text for calculations. **c** Concentration of copper (Cu) in the fluid phase (emitted gas plume) supplied by sulfide resorption, shown for a range of melt-vapor partition coefficients and the upper and lower bounds of sulfide volume percent. Literature values of experimental vapor-melt partition coefficients (Kd) for Cu are annotated (= 48, Guo and Audetat[146]; = 510, Zajacz et al.[147], = 0.0023, Zelenski et al.[145]); see main text for discussion. **d** Conceptual diagram illustrating proposed elemental exchange between sulfide, silicate melt, and exsolved magmatic vapor phase.

Contribution of sulfide breakdown to sulfur and chalcophile metal emissions

On resorption, sulfides can release their sulfur and chalcophile trace element cargo back into the melt-vapor system, upon which they are degassed according to melt-vapor partitioning, with elements partitioning into the exsolved vapor phase according to their volatility[47]. However, metal and metalloid trace element assemblages measured in several volcanic plumes instead more closely reflect sulfide-melt partitioning behavior[63,76], suggesting that chalcophile elements sequestered in an immiscible sulfide phase may modulate the emission of these elements to the atmosphere.

If we consider a representative range of sulfide volume fraction predicted by SCSS models at 6.5 wt% MgO, (1σ error bounds of 0.01–0.08 vol%, equivalent to 0.02–0.12 wt%; Fig. 9c), and assume that S released from the sulfide during late stage degassing partitions entirely into the vapor phase, then we may calculate the amount of outgassed sulfur supplied theoretically by complete sulfide resorption (Eqs. 7–9, Fig. 10a):

$$S_{resorption} = S_{sf} \times \left(\frac{V_{sf} R}{100}\right) \quad (7)$$

where $S_{resorption}$ = sulfur supplied to the melt-vapor system by sulfide resorption (wt%), S_{sf} = bulk S composition in sulfide (wt%), R is the density ratio of sulfide to silicate melt (4200/2804 kg m^{-3};[105,122]), and V_{sf} = volume of sulfide resorbed (%). We also calculate the amount of S lost from the melt through degassing ($S_{degassed}$, wt%) from the S content of melt inclusions (S_{MI}, wt%), representative of the undegassed melt S concentration, and the S content of matrix glass (S_{glass}, wt%), representative of the residual S concentration in the melt after degassing to 1 atm:

$$S_{degassed} = S_{MI} - S_{glass} \quad (8)$$

From these two parameters, we calculate the % contribution from sulfide resorption to the total S flux (Fig. 10b):

$$C(\%) = \left(\frac{S_{resorption}}{(S_{resorption} + S_{degassed})}\right) \times 100 \quad (9)$$

We note that our SCSS models of sulfide volume % assume no removal (settling) of sulfides during crystallization, which seems a reasonable first-order assumption given the agreement between modeled and measured sulfide volume percent from the early erupted sample (Fig. 9c).

Taking the average sulfur bulk composition measured in Holuhraun sulfides (33.6 wt%) and the total sulfur degassed from the melt (0.16 [undegassed]– 0.04 [degassed] wt% = 0.12 wt%), then resorption of 0.02 and 0.12 wt% sulfide would contribute 4% and 27% of the total sulfur emissions, respectively. If we consider the total sulfur dioxide mass loading over the eruption to be 9.6 ± 2.9–4.8 Tg SO_2[92], then this implies that up to ~2.6 Tg SO_2 may have been supplied by sulfide resorption. The mass fraction of sulfide, both forming and resorbing, may vary in time and space in response to changes in eruption dynamics and magma supply. We model the potential contributions to S outgassing from sulfide breakdown over a range of sulfide volume percent in Fig. 10, considering the 2σ uncertainty on the average sulfide bulk composition. Sulfide breakdown, even in relatively small amounts, may therefore be a plausible mechanism to supply considerable amounts of sulfur to basaltic volcanic plumes (as discussed by Wieser et al.[47] for Kīlauean eruptions).

Sulfide breakdown would also be expected to release Cu and other chalcophile metals into the melt-vapor system (Fig. 10d). However, in contrast to S, which is highly volatile, Cu is much less volatile[29,145]. Unless the sulfide is in direct contact with the vapor, the partitioning behavior of Cu between melt and exsolved fluids will determine the proportion of the total Cu supplied by resorption that may be outgassed. From the average Cu

composition measured in sulfides (17.4 wt%), resorption of 0.08 vol% sulfide would supply 209 ppm (0.02 wt%) Cu to the melt-vapor system. Vapor-melt partition coefficients, $D_{vapor\text{-}melt}$, of 48 (ref. 146) and 510 (ref. 147) have been determined experimentally for Cu, and would imply only 6 ppm and <1 ppm (of the total 209 ppm Cu added) would remain in the melt, respectively. However, Cu (and also Ag) speciates strongly with chloride and therefore its volatility is limited by the salinity of exsolved fluids[148–150]. These experiments yielding high $D_{vapor\text{-}melt}$ values were performed with high chlorine concentrations in the aqueous fluid and therefore likely overestimate $D_{vapor\text{-}melt}$ for Cl-poor melts (e.g., Icelandic basalts,[24,151]). For example, the SO_2/HCl molar ratios measured in the 2014–15 Holuhraun gas plume was 46–79[92], compared to substantially lower ratios in more Cl-rich arc volcanic plumes (e.g., 0.3–8.8 Stromboli, Italy; 1.5–2.6 Masaya, Nicaragua; 3–5.3 Ambrym, Vanuatu;[152,153]).

We model the expected Cu concentration in the fluid phase derived from sulfide resorption for a range of $D_{vapor\text{-}melt}$ values in Fig. 10c. We find that for $D_{vapor\text{-}melt} > 10$, the proportion remaining in the melt becomes vanishingly small, and there is very little difference in the amount released as $D_{vapor\text{-}melt}$ increases further. However, Zelenski et al.[145] present a vapor-melt partition coefficient of 0.0023 for Cu (in rift/hotspot settings) derived empirically from high-quality volcanic gas and whole rock compositions. This much lower K_D implies that Cu has a relatively low volatility in ocean island basalts and therefore that much of the Cu added back into the melt-vapor system by sulfide resorption would remain in the melt. A key independent constraint on $D_{vapor\text{-}melt}$ comes from our measured Cu concentrations of 161 ± 22 ppm [2σ] and 182 ± 38 ppm [2σ] in the matrix glass of quenched pyroclasts from H14 and EI, respectively (Supplementary Fig. 9). These values in the degassed melt are incompatible with those predicted for high vapor-melt partitioning behavior for realistic initial Cu contents in ocean island basalts. Based on chalcophile element systematics in melt inclusions and matrix glasses at Kilauea volcano (another low-H_2O, low-Cl basaltic system), Wieser et al.[47] also suggest that most of the Cu released from sulfide breakdown remains in the melt. In contrast to Cu, outgassing of elements that have a relatively low abundance in silicate melts but which are both volatile and partition strongly into sulfide liquids (e.g., Se and Te) will be highly sensitive to a sulfide phase breaking down; even small additions to the melt would be expected to produce a large change in the amount released to the volcanic plume.

Evidence for magmatic sulfides is widespread—either in the form of visible sulfide globules or more cryptically in trace element geochemical records—in the erupted products of basaltic fissure eruptions in ocean island settings, including Réunion[84], El Hierro (Canary Islands[154]), Mangaia (Cook Islands[155]), 2011 Grímsvötn (Iceland[75]), Hverfjall Fires (Iceland,[120]), and various eruptions at Kīlauea including 1959 Kīlauea Iki, 1969–1974 Mauna Ulu, 1955 and 1977 East Rift Zone[47,156–159]. However, the 2014–15 Holuhraun eruption appears unique in the larger abundance of sulfides preserved within matrix glasses, compared to the very small number of sulfides present in Kīlauea matrix glasses[47]. It could be expected that eruptions where sulfide resorption has proceeded to almost completion would yield different degassing signatures to those where there are still numerous sulfides remaining in the melt on eruption. Once all available sulfide is exhausted (i.e., not isolated within intact melt inclusions), trace element outgassing may proceed according to fluid-melt partitioning. The paucity of remaining sulfides at Kilauea may explain why metals appear to be outgassed in proportions that are poorly correlated with sulfide-melt K_D values[47]. Similar signatures would be expected for basaltic eruptions which are not sulfide saturated upon eruption, perhaps because they are more oxidized, or experienced open-system degassing, lava drainback and recycling[44].

In contrast, eruptions which are sulfide saturated and possess sulfides that continue to break down throughout the degassing interval may experiencing buffering of the chalcophile element contents in the melt by the presence of sulfides, or direct transfer of metals from sulfide to fluid, resulting in a different geochemical fingerprint versus the sulfide-free scenario. It is also worth considering the effects of kinetics on degassing signatures. It is well established that H, C and S are fractionated from one another during volcanic degassing because of the vastly different diffusion rates of these elements through the melt[160]. In fact, kinetic effects are vital for extending the interval over which sulfides are resorbed during degassing, and preserving the high S concentrations seen in erupted matrix glasses. Kinetically-limited sulfide breakdown may establish large gradients in the silicate melt of chalcophile elements with high sulfide-melt K_Ds but more sluggish diffusion rates. Chalcophile elements can only be degassed based on silicate-vapor partition coefficients if all elements can diffuse to the nearest bubble as quickly as they are degassed. Thus, emitted metal signatures in the presence of abundant resorbing sulfides may also be strongly modulated by elemental diffusion rates in the silicate melt, as has been shown in experiments[161,162]. Measurements of sulfide-liquid partition coefficients, liquid-vapor partition coefficients, and elemental diffusion coefficients in relatively reduced, H_2O-poor OIB-type basaltic melts will play a key role in future advances in understanding the complex exchange of chalcophile elements between melt, sulfide and vapor phases during degassing.

Kinetic effects also mean that that the sulfide systematics preserved in quenched tephra, such as those examined here, are not the end of the story. Further degassing of sulfur and volatile trace elements takes place during (a) lava fountaining and post-fragmentation expansion of scoria lapilli[120,163–165], and (b) lava flow, emplacement, and slow cooling[24,44,92,98,165]. In Iceland, delayed post-eruptive degassing is demonstrated clearly in petrological records; for example, while 1185 ppm S is released at the vents, a further 140 and 155 ppm S is degassed during lava transport and post-emplacement, respectively[24]. Similarly, during the 2018 Kilauea eruption, petrological observations and remote sensing measurements suggest that between 10 and 45% of the total magmatic sulfur degassed during surface lava flows[44]. If sulfide preservation in quenched tephra close to the vent is a product of slow sulfur diffusion rates, then we may expect resorption to have progressed to completion in those Holuhraun melts erupted effusively. A compelling hypothesis to explore is therefore whether the emitted chalcophile trace element assemblage in the plume varies systematically between the vent and progressive distances down flow in a way that can be linked explicitly to the exhaustion of sulfides.

Conclusions

Sulfide saturation occurs in many magmas feeding basaltic eruptions in ocean island and MORB settings globally, with implications for the availability of sulfur and chalcophile trace elements within silicate melts. However, textural and geochemical evidence documenting sulfide breakdown and resorption is commonly erased or overprinted in erupted products. Sulfide globules in rapidly quenched tephra erupted during the 2014–15 Holuhraun eruption exhibit variations in texture and composition in both time and space that describe the complete life cycle of sulfide nucleation, growth, segregation, and ultimately resorption, presenting a valuable opportunity to explore sulfide breakdown, preserved in progress. By underpinning textural and geochemical observations of sulfides, sulfide-bearing minerals and glasses, with modeling constraints, we argue that rapid, late-stage resorption of sulfide associated with the onset of sulfur degassing may modulate the emission of sulfur and chalcophile elements to the atmosphere and surface environment in magmas that are sulfide-saturated at the onset of sulfur degassing.

1. Sulfide nucleation in the Holuhraun melt began at ~8 wt% MgO, when sulfide saturation was reached, and continued until the onset of sulfur degassing at ~6.5 wt% MgO, whereupon partitioning of dissolved sulfur from the melt into an exsolved vapor phase drives the melt rapidly towards sulfide undersaturation. The gradual divergence between fractional crystallization and sulfide content at sulfide saturation ($SCSS^{2-}$) model trajectories suggest that sulfides may not have become abundant in the melt until <7 wt% MgO.
2. Sulfide globules are observed within matrix glass, attached to the surfaces of bubbles and crystals and, less commonly, as inclusions within minerals. Sulfides are preserved preferentially in confined geometries within and between crystals and crystal clusters, likely due to kinetic effects that impede sulfur loss from the melt and maintain local sulfide saturation on eruption. Textural associations between sulfides and

crystals, combined with the observation that sulfide liquids appear to wet crystal surfaces, hint that crystal attachment may be a more important mechanism for transporting sulfides than previously thought.

3. The proportion of sulfides exhibiting breakdown textures increases from <10% at the eruption onset (August 2014) to ~50% in November 2014 and January 2015. We suggest that the preservation of sulfide may be, at least in part, coupled to the magma effusion rate, which reduced throughout the eruption[91,139]. Later erupted samples may have spent longer at shallow depths, where extensive sulfur loss through degassing had begun —so there was additional time for sulfide breakdown and resorption to proceed.
4. Mineral-sulfide associations describe a protracted interval of melt evolution where sulfides were present either coincident with or subsequent to the growth of clinopyroxene, olivine, plagioclase in equilibrium with MgO contents ~8, 7–8 and <6.5 wt% respectively. The relatively evolved compositions of sulfide-bearing plagioclase-clinopyroxene-olivine crystal clusters suggest crystallization during lateral magma transport within the dike, perhaps re-entrained from the cooler dike margins.
5. Sulfide resorption, even in relatively small amounts, presents a plausible mechanism to supply substantial amounts of sulfur and chalcophile elements to basaltic volcanic plumes. Mass balance modeling suggests that resorption of 0.08 vol% (0.12 wt%) sulfide could account for an additional ~0.04 wt% S and 0.01 to 0.02 wt% Cu in the melt, which, when degassed, would account for ~27% of the total Holuhraun sulfur emissions and non-negligible Cu emissions, depending on the vapor-melt partition coefficient.
6. The speciation behavior of chalcophile elements likely has a strong control over whether those elements contribute to the outgassed plume assemblage or remain in the melt upon resorption. While Cu, for example, has a relatively low volatility in low-H_2O, low-Cl tholeiitic basalts, outgassing of elements that are highly volatile, highly chalcophile, and have a low abundance in silicate melts (e.g., Se, Te) are particularly sensitive to sulfide resorption; even small additions to the melt will translate to large changes in volcanic plume concentrations. However, we highlight the need for further experimental data on trace element fluid-melt partitioning in reduced, Cl-poor systems relevant to Kīlauea and Iceland, and on the diffusion rates of these elements in water-poor basaltic melts.
7. Contrasting sulfide systematics between Kīlauea and Holuhraun may reflect (a) differences in the major element contents of primary magmas at Iceland and Hawai'i and therefore crystallization trajectories during differentiation, and (b) that sulfide resorption proceeded to near-completion in many Kīlauean melts that reached sulfide saturation, while both textural and geochemical evidence suggest that at Holuhraun, on eruption at the vent, it had not. Continued degassing and slow cooling of effusive lavas may have recorded the resorption process to completion, however. Once all available sulfide is exhausted, trace element outgassing will proceed according to fluid-melt partitioning, potentially masking geochemical signatures of sulfide resorption in either erupted products or plume measurements.

Further constraints on the relative timing of sulfide nucleation, growth and resorption are critical to our ability to reconstruct the sulfur and trace element yields from past eruptions or to forecast anticipated yields from future eruptions for a range of magma compositions; the latter is particularly important for generating timely and accurate environmental hazard assessments for trace element exposure from volcanic plumes[17,18,166,167].

Methods

Textural characterization

We identified sulfides from backscattered electron (BSE) images acquired using a FEI Quanta 650FEG scanning electron microscope (SEM) at the University of Cambridge, operating at working distances of 13–15 mm and a 15 kV accelerating voltage. We imaged individual sulfide globules at a magnification that yielded ~10^5 pixels/sulfide (at a resolution of 1024 × 798 and 10 µs integration time) to ensure that uncertainties on sulfide area and shape measurements are independent of size. BSE images were thresholded using ImageJ software (http://imagej.nih.gov/ij/) and analysed using an open-source shape macro for ImageJ[103,168].

We measured the size distribution of sulfide globules for sample H14 based on SEM mosaics of four lapilli cross-sections. Measured 2D areas were converted into circular equivalent diameters (Eq. 10) assuming a spherical globule morphology and binned into geometric size classes.

$$D_{eq} = 2\sqrt{\pi A} \tag{10}$$

where A is the measured area of each sulfide. The number of sulfides in each size class was normalized by the total vesicle- and phenocryst-free melt area to give the 2D number density, N_a (mm^{-2}). We calculated the equivalent 3D number density, N_v (mm^{-3}) and population density (mm^{-4}) using stereological procedures embedded within CSDCorrections[169]; http://www.uqac.ca/mhiggins/csdcorrections.html), assuming a spheroidal geometry. The total sulfide number density (SND, mm^{-3}) is the sum of N_v across all size classes. Population density is expressed as ln(n) vs size (L), where n is the slope of the cumulative N_v distribution with units of number per size class per volume; the characteristic size (L_D) of the distribution is calculated from Eq. 11:

$$L_D = -\frac{1}{s} \tag{11}$$

where s is the slope of the regression. The sulfide volume distribution is calculated by multiplying N_v for each size class by the volume of a sphere with a diameter equal to the midpoint of the corresponding size class and converted to sulfide volume fraction by expressing the volume within each size class as a percentage of the total sulfide volume. The sulfide volume percent refers to the total volume of sulfide as a percentage of the total vesicle- and crystal-free melt volume.

Major and trace element compositions

Major, minor and volatile (S and Cl) element concentrations in matrix glass, sulfides, and silicate mineral phases for H14, MSR and EI were measured on carbon-coated polished grain mounts using a Cameca SX100 electron microprobe (EPMA) at the University of Cambridge, UK. Full details of analytical conditions are presented in Supplementary Note 1 and Supplementary Dataset 1.

For coarse-grained and zoned sulfide globules (i.e., compositional zones » beam diameter), we analysed the chemical composition of each phase separately using wavelength-dispersive X-ray spectroscopy (WDS). We then reconstructed the bulk composition of the sulfide globule by calculating a weighted average based on the 2D area proportion of each sulfide phase measured from BSE SEM images. We note that the large analytical volume of EPMA at depth in the sample may introduce an unquantified uncertainty to the measured composition of smaller compositional domains. For sulfide globules with a fine-grained texture, the compositional variation is at a scale smaller than the beam size and interaction volume. Here, unweighted averages of one to three analysis points (depending on the sulfide size) were used to determine bulk composition, with each analysis representing an average composition over the incident beam area and interaction volume. Additionally, we acquired energy-dispersive X-ray spectroscopy (EDS) maps of sulfide globules using two 3||60 Bruker flash detectors (90 kcps) for acquisition times of 12–15 min. Sulfide compositions (both bulk compositions and individual domains) were determined from EDS spectra using Esprit2.1 software and the PhiRhoZ quantification (standardless). This approach has been shown to recreate the S-Cu-Ni-Fe composition of sulfide standards measured by EPMA within ±5–10%[47].

We analysed trace element concentrations in matrix glasses from samples H14 and EI by laser ablation inductively coupled plasma mass spectrometry (LA-ICP-MS) at the School of Environment, Earth and

Ecosystem Sciences at the Open University using a Photon Machines Analyte G2 193 nm excimer laser system coupled to an Agilent 8800 ICP-QQQ and following techniques outlined in[82,170]; see Supplementary Note 2 for analytical metadata. We used a laser spot size diameter of 50 and 65 µm for all elements, positioned manually for each analysis to ensure no overlap with any mineral phases or small visible sulfide globules, and a repetition rate of 10 Hz and a laser fluence of 3.63 J/cm^2. Sample aerosols were transported in a He atmosphere (0.9 l/min) with 5 ml/min N_2 added via a y-connector downstream to increase sensitivity. The surface of the glass was pre-ablated prior to analysis to remove surface contamination. Backgrounds were measured for 30 s prior to each analysis, followed by 30 s of signal and 50 s of washout. NIST-SRM 612 reference material was used for external calibration and ^{29}Si for internal calibration of trace element data. BCR-2G was used as the secondary standard to monitor precision and accuracy. The isobaric interference from ^{115}Sn on ^{115}In was corrected following the protocol outlined in Jenner and O'Neill[170].

Data availability

Geochemical and textural data are provided in Supporting Dataset 1, and archived on Zenodo (https://zenodo.org/doi/10.5281/zenodo.10471904).

Code availability

Jupyter Notebooks used for modeling are archived at Zenodo (https://zenodo.org/doi/10.5281/zenodo.10471904), also available through GitHub https://github.com/PennyWieser/Holuhraun_Sulfide_Resorption_CommsEE.

Received: 28 October 2022; Accepted: 31 January 2024;
Published online: 30 March 2024

References

1. Brimblecombe, P. & Lein, A. Y. *Evolution of the global biogeochemical sulphur cycle*. (John Wiley and Sons Inc., 1989).
2. Fike, D. A., Bradley, A. S. & Rose, C. V. Rethinking the ancient sulfur cycle. *Annu. Rev. Earth Planet. Sci.* **43**, 593–622 (2015).
3. Alt, J. C., Shanks, W. C. & Jackson, M. C. Cycling of sulfur in subduction zones: the geochemistry of sulfur in the Mariana Island Arc and back-arc trough. *Earth Planet. Sci. Lett.* **119**, 477–494 (1993).
4. de Moor, J. M., Fischer, T. P. & Plank, T. Constraints on the sulfur subduction cycle in Central America from sulfur isotope compositions of volcanic gases. *Chem. Geol.* **588**, 120627 (2022).
5. Evans, K. A. The redox budget of subduction zones. *Earth-Sci. Rev.* **113**, 11–32 (2012).
6. Li, J.-L. et al. Uncovering and quantifying the subduction zone sulfur cycle from the slab perspective. *Nat. Commun.* **11**, 514 (2020).
7. Iacono-Marziano, G., Le Vaillant, M., Godel, B. M., Barnes, S. J. & Arbaret, L. The critical role of magma degassing in sulphide melt mobility and metal enrichment. *Nat. Commun.* **13**, 2359 (2022).
8. Sun, W. et al. Porphyry deposits and oxidized magmas. *Ore Geol. Rev.* **65**, 97–131 (2015).
9. Wilkinson, J. J. Triggers for the formation of porphyry ore deposits in magmatic arcs. *Nat. Geosci.* **6**, 917–925 (2013).
10. Carroll, M. R. & Rutherford, M. J. Sulfur speciation in hydrous experimental glasses of varying oxidation state; results from measured wavelength shifts of sulfur X-rays. *Am. Mineralo.* **73**, 845–849 (1988).
11. Jugo, P. J. Sulfur content at sulfide saturation in oxidized magmas. *Geology* **37**, 415–418 (2009).
12. Wilke, M. et al. The origin of S4+ detected in silicate glasses by XANES. *Am. Mineralo.* **93**, 235–240 (2008).
13. Lesne, P. et al. Experimental simulation of closed-system degassing in the system Basalt–H2O–CO2–S–Cl. *J. Petrol.* **52**, 1737–1762 (2011).
14. Moretti, R. & Papale, P. On the oxidation state and volatile behavior in multicomponent gas–melt equilibria. *Chem. Geol.* **213**, 265–280 (2004).
15. Webster, J. D. & Botcharnikov, R. E. Distribution of sulfur between melt and fluid in S-O-H-C-Cl-Bearing Magmatic systems at shallow crustal pressures and temperatures. *Rev. Mineral. Geochem.* **73**, 247–283 (2011).
16. Wieser, P. E. & Jenner, F. E. Chalcophile elements: systematics and relevance. in *Reference Module in Earth Systems and Environmental Sciences* B9780081029084000928 (Elsevier, 2020). https://doi.org/10.1016/B978-0-08−102908-4.00092-8.
17. Ilyinskaya, E. et al. Rapid metal pollutant deposition from the volcanic plume of Kīlauea, Hawai'i. *Commun. Earth Environ.* **2**, 1–15 (2021).
18. Ilyinskaya, E. et al. Understanding the environmental impacts of large fissure eruptions: aerosol and gas emissions from the 2014–2015 Holuhraun eruption (Iceland). *Earth Planet. Sci. Lett.* **472**, 309–322 (2017).
19. Kern, C. et al. Quantifying gas emissions associated with the 2018 rift eruption of Kīlauea Volcano using ground-based DOAS measurements. *Bull. Volcanol.* **82**, 55 (2020).
20. Mather, T. A. et al. Halogens and trace metal emissions from the ongoing 2008 summit eruption of Kīlauea volcano, Hawai'i. *Geochim. et Cosmochim. Acta* **83**, 292–323 (2012).
21. Mather, T. A. & Schmidt, A. Environmental effects of volcanic volatile fluxes from subaerial large igneous provinces. in *Large Igneous Provinces* 103–116 (American Geophysical Union (AGU), 2021). https://doi.org/10.1002/9781119507444.ch4.
22. Self, S., Widdowson, M., Thordarson, T. & Jay, AnneE. Volatile fluxes during flood basalt eruptions and potential effects on the global environment: a Deccan perspective. *Earth Planet. Sci. Lett.* **248**, 518–532 (2006).
23. Thordarson, T., Miller, D. J., Larsen, G., Self, S. & Sigurdsson, H. New estimates of sulfur degassing and atmospheric mass-loading by the 934 AD Eldgjá eruption, Iceland. *J. Volcanol. Geotherm. Res.* **108**, 33–54 (2001).
24. Thordarson, T., Self, S., Óskarsson, N. & Hulsebosch, T. Sulfur, chlorine, and fluorine degassing and atmospheric loading by the 1783–1784 AD Laki (Skaftár Fires) eruption in Iceland. *Bull. Volcanol.* **58**, 205–225 (1996).
25. Thordarson, T. & Self, S. Sulfur, chlorine and fluorine degassing and atmospheric loading by the Roza eruption, Columbia River Basalt Group, Washington, USA. *J. Volcanol. Geotherm. Res.* **74**, 49–73 (1996).
26. Allard, P. et al. Acid gas and metal emission rates during long-lived basalt degassing at Stromboli Volcano. *Geophys. Res. Lett.* **27**, 1207–1210 (2000).
27. Edmonds, M., Mason, E. & Hogg, O. Volcanic outgassing of volatile trace metals. *Annu. Rev. Earth Planet. Sci.* **50**, 79–98 (2022).
28. Mandon, C. L., Christenson, B. W., Schipper, C. I., Seward, T. M. & Garaebiti, E. Metal transport in volcanic plumes: a case study at White Island and Yasur volcanoes. *J. Volcanol. Geothermal Res.* **369**, 155–171 (2019).
29. Mason, E. et al. Volatile metal emissions from volcanic degassing and lava–seawater interactions at Kīlauea Volcano, Hawai'i. *Commun. Earth Environ.* **2**, 1–16 (2021).
30. Schmidt, A. et al. Excess mortality in Europe following a future Laki-style Icelandic eruption. *Proc. Natl. Acad. Sci.* **108**, 15710–15715 (2011).
31. Whitty, R. C. W. et al. Spatial and temporal variations in SO<inf>2</inf> and PM<inf>2.5</inf> Levels Around Kīlauea Volcano, Hawai'i During 2007–2018. (2020) https://doi.org/10.17863/CAM.48768.
32. Robock, A. Volcanic eruptions and climate. *Rev. Geophys.* **38**, 191–219 (2000).
33. Schmidt, A. et al. Selective environmental stress from sulphur emitted by continental flood basalt eruptions. *Nat. Geosci.* **9**, 77–82 (2016).
34. Thordarson, T., Rampino, M., Keszthelyi, L. P. & Self, S. Effects of megascale eruptions on Earth and Mars. in *Preservation of Random*

Megascale Events on Mars and Earth: Influence on Geologic History (eds. Keszthelyi, L. P. & Chapman, M. G.) (Geological Society of America, 2009).
35. Thordarson, T. & Self, S. Atmospheric and environmental effects of the 1783–1784 Laki eruption: a review and reassessment. *J. Geophys. Res.: Atmos.* **108**, AAC 7-1–AAC 7-29 (2003).
36. Falcone, E. E. et al. Impact of acidic volcanic emissions on ash leaching and on the bioavailability and mobility of trace metals in soils of Mt. Etna. *Ital. J. Geosci.* **140**, 57–78 (2021).
37. Gislason, S., Stefansdottir, G. & Pfeffer, M. A. Environmental pressure from the 2014–15 eruption of Bárðarbunga volcano, Iceland. *Geochem. Perspect. Lett.* **1**, 84–93 (2015).
38. Gíslason, S. R. et al. Effects of volcanic eruptions on the CO2 content of the atmosphere and the oceans: the 1996 eruption and flood within the Vatnajökull Glacier, Iceland. *Chem. Geol.* **190**, 181–205 (2002).
39. Liotta, M. et al. Magmatic signature in acid rain at Masaya volcano, Nicaragua: Inferences on element volatility during lava lake degassing. *Chem. Geol.* **585**, 120562 (2021).
40. Moune, S., Gauthier, P.-J., Gislason, S. R. & Sigmarsson, O. Trace element degassing and enrichment in the eruptive plume of the 2000 eruption of Hekla volcano, Iceland. *Geochim. et Cosmochim. Acta* **70**, 461–479 (2006).
41. Ragnarsdottir, K. V., Gislason, S. R., Thorvaldsson, T., Kemp, A. J. & Andresdottir, A. Ejection of trace metals from volcanoes. *Mineral. Magazine* **58**, 752–753 (1994).
42. Rodríguez-Hernández, Á. et al. Impact of chemical elements released by the volcanic eruption of La Palma (Canary Islands, Spain) on banana agriculture and European consumers. *Chemosphere* **293**, 133508 (2022).
43. Stefánsson, A. et al. Major impact of volcanic gases on the chemical composition of precipitation in Iceland during the 2014–2015 Holuhraun eruption. *J. Geophys. Res.: Atmos.* **122**, 1971–1982 (2017).
44. Lerner, A. H. et al. The petrologic and degassing behavior of sulfur and other magmatic volatiles from the 2018 eruption of Kīlauea, Hawai'i: melt concentrations, magma storage depths, and magma recycling. *Bull. Volcanol.* **83**, 43 (2021).
45. Thordarson, T., Self, S., Miller, D. J., Larsen, G. & Vilmundardóttir, E. G. Sulphur release from flood lava eruptions in the Veidivötn, Grímsvötn and Katla volcanic systems, Iceland. *Geol. Soc. Lond. Special Publications* **213**, 103–121 (2003).
46. Vidal, C. M. et al. The 1257 Samalas eruption (Lombok, Indonesia): the single greatest stratospheric gas release of the Common Era. *Sci. Rep.* **6**, 34868 (2016).
47. Wieser, P. E., Jenner, F., Edmonds, M., Maclennan, J. & Kunz, B. E. Chalcophile elements track the fate of sulfur at Kīlauea Volcano, Hawai'i. *Geochim.et Cosmochim. Acta* **282**, 245–275 (2020).
48. Liu, Y., Samaha, N.-T. & Baker, D. R. Sulfur concentration at sulfide saturation (SCSS) in magmatic silicate melts. *Geochim. et Cosmochim. Acta* **71**, 1783–1799 (2007).
49. Mavrogenes, J. A. & O'Neill, H. St. C. The relative effects of pressure, temperature and oxygen fugacity on the solubility of sulfide in mafic magmas. *Geochim. et Cosmochim. Acta* **63**, 1173–1180 (1999).
50. O'Neill, H. St. C. The thermodynamic controls on sulfide saturation in silicate melts with application to ocean floor basalts. in *Magma Redox Geochemistry* 177–213 (American Geophysical Union (AGU), 2021). https://doi.org/10.1002/9781119473206.ch10.
51. Smythe, D. J., Wood, B. J. & Kiseeva, E. S. The S content of silicate melts at sulfide saturation: new experiments and a model incorporating the effects of sulfide composition. *Am. Mineral.* **102**, 795–803 (2017).
52. Patten, C., Barnes, S.-J. & Mathez, E. A. Textural variations in morb sulfide droplets due to differences in crystallization history. *Can. Mineral.* **50**, 675–692 (2012).
53. Halldórsson, S. A. et al. Petrology and geochemistry of the 2014–2015 Holuhraun eruption, central Iceland: compositional and mineralogical characteristics, temporal variability and magma storage. *Contrib. Mineral. Petrol.* **173**, 64 (2018).
54. Kiseeva, E. S. & Wood, B. J. The effects of composition and temperature on chalcophile and lithophile element partitioning into magmatic sulphides. *Earth Planet. Sci. Lett.* **424**, 280–294 (2015).
55. Kiseeva, E. S. & Wood, B. J. A simple model for chalcophile element partitioning between sulphide and silicate liquids with geochemical applications. *Earth Planet. Sci. Lett.* **383**, 68–81 (2013).
56. Li, Y. & Audétat, A. Partitioning of V, Mn, Co, Ni, Cu, Zn, As, Mo, Ag, Sn, Sb, W, Au, Pb, and Bi between sulfide phases and hydrous basanite melt at upper mantle conditions. *Earth Planet. Sci. Let.* **355–356**, 327–340 (2012).
57. Patten, C., Barnes, S.-J., Mathez, E. A. & Jenner, F. E. Partition coefficients of chalcophile elements between sulfide and silicate melts and the early crystallization history of sulfide liquid: LA-ICP-MS analysis of MORB sulfide droplets. *Chem. Geol.* **358**, 170–188 (2013).
58. Barnes, S. J. Komatiite-hosted nickel sulfide deposits: geology, geochemistry, and genesis. In *Nickel Deposits of the Yilgarn Craton: Geology, Geochemistry, and Geophysics Applied to Exploration* (ed. Barnes, S. J.) vol. 13 0 (Society of Economic Geologists, 2006).
59. Berlo, K., van Hinsberg, V. J., Vigouroux, N., Gagnon, J. E. & Williams-Jones, A. E. Sulfide breakdown controls metal signature in volcanic gas at Kawah Ijen volcano, Indonesia. *Chem. Geol.* **371**, 115–127 (2014).
60. Chen, Z. et al. Magmatic sulfide saturation and dissolution in the basaltic andesitic magma from the Yaeyama Central Graben, southern Okinawa Trough. *Lithos* **388–389**, 106082 (2021).
61. Edmonds, M. & Mather, T. A. Volcanic sulfides and outgassing. *Elements* **13**, 105–110 (2017).
62. Mungall, J. E., Brenan, J. M., Godel, B., Barnes, S. J. & Gaillard, F. Transport of metals and sulphur in magmas by flotation of sulphide melt on vapour bubbles. *Nat. Geosci.* **8**, 216–219 (2015).
63. Nadeau, O., Williams-Jones, A. E. & Stix, J. Sulphide magma as a source of metals in arc-related magmatic hydrothermal ore fluids. *Nat. Geosci.* **3**, 501–505 (2010).
64. Vlastélic, I. et al. Origin and fate of sulfide liquids in hotspot volcanism (La Réunion): Pb isotope constraints from residual Fe–Cu oxides. *Geochim. et Cosmochim. Acta* **194**, 179–192 (2016).
65. Craig, J. R. & Kullerud, G. Phase Relations in the Cu-Fe-Ni-S System and Their Application to Magmatic Ore Deposits. in *Magmatic Ore Deposits* (ed. Wilson, H. D. B.) vol. 4 0 (Society of Economic Geologists, 1969).
66. Ebel, D. S. & Naldrett, A. J. Crystallization of sulfide liquids and the interpretation of ore composition. *Can. J. Earth Sci.* **34**, 352–365 (1997).
67. Ebel, D. S. & Naldrett, A. J. Fractional crystallization of sulfide ore liquids at high temperature. *Econ. Geol.* **91**, 607–621 (1996).
68. Kullerud, G., Yund, R. A. & Moh, G. H. Phase Relations in the Cu-Fe-S, Cu-Ni-S, and Fe-Ni-S Systems*. in *Magmatic* Ore *Deposits* (ed. Wilson, H. D. B.) vol. 4 0 (Society of Economic Geologists, 1969).
69. Naldrett, A. J., Craig, J. R. & Kullerud, G. The central portion of the Fe-Ni-S system and its bearing on pentlandite exsolution in iron-nickel sulfide ores. *Econ. Geol.* **62**, 826–847 (1967).
70. Helmy, H. M., Ballhaus, C., Wohlgemuth-Ueberwasser, C., Fonseca, R. O. C. & Laurenz, V. Partitioning of Se, As, Sb, Te and Bi between monosulfide solid solution and sulfide melt – Application to magmatic sulfide deposits. *Geochim. et Cosmochim. Acta* **74**, 6174–6179 (2010).
71. Mungall, J. E., Andrews, D. R. A., Cabri, L. J., Sylvester, P. J. & Tubrett, M. Partitioning of Cu, Ni, Au, and platinum-group elements between monosulfide solid solution and sulfide melt under

controlled oxygen and sulfur fugacities. *Geochim. et Cosmochim. Acta* **69**, 4349–4360 (2005).
72. Helmy, H. M. et al. Evolution of magmatic sulfide liquids: how and when base metal sulfides crystallize? *Contrib. Mineral. Petrol.* **176**, 107 (2021).
73. Devine, J. D., Sigurdsson, H., Davis, A. N. & Self, S. Estimates of sulfur and chlorine yield to the atmosphere from volcanic eruptions and potential climatic effects. *J. Geophys. Res.: Solid Earth* **89**, 6309–6325 (1984).
74. Gauthier, P.-J., Sigmarsson, O., Gouhier, M., Haddadi, B. & Moune, S. Elevated gas flux and trace metal degassing from the 2014–2015 fissure eruption at the Bárðarbunga volcanic system, Iceland. *J. Geophys. Res.: Solid Earth* **121**, 1610–1630 (2016).
75. Sigmarsson, O. et al. The sulfur budget of the 2011 Grímsvötn eruption, Iceland. *Geophys. Res. Lett.* **40**, 6095–6100 (2013).
76. Edmonds, M., Mather, T. A. & Liu, E. J. A distinct metal fingerprint in arc volcanic emissions. *Nat. Geosci.* **11**, 790–794 (2018).
77. Chen, K. et al. Sulfide-bearing cumulates in deep continental arcs: the missing copper reservoir. *Earth Planet. Sci. Lett.* **531**, 115971 (2020).
78. Jenner, F. E. Cumulate causes for the low contents of sulfide-loving elements in the continental crust. *Nat. Geosci.* **10**, 524–529 (2017).
79. Jenner, F. E., O'Neill, H. S. T. C., Arculus, R. J. & Mavrogenes, J. A. The magnetite crisis in the evolution of Arc-related magmas and the initial concentration of Au, Ag and Cu. *J. Petrol.* **51**, 2445–2464 (2010).
80. Park, J.-W. et al. Chalcophile element fertility and the formation of porphyry Cu ± Au deposits. *Miner. Deposita.* **54**, 657–670 (2019).
81. Jenner, F. E. et al. The competing effects of sulfide saturation versus degassing on the behavior of the chalcophile elements during the differentiation of hydrous melts. *Geochem. Geophys. Geosyst.* **16**, 1490–1507 (2015).
82. Reekie, C. D. J. et al. Sulfide resorption during crustal ascent and degassing of oceanic plateau basalts. *Nat. Commun.* **10**, 82 (2019).
83. Tattitch, B., Chelle-Michou, C., Blundy, J. & Loucks, R. R. Chemical feedbacks during magma degassing control chlorine partitioning and metal extraction in volcanic arcs. *Nat. Commun.* **12**, 1774 (2021).
84. Collins, S. J., Maclennan, J., Pyle, D. M., Barnes, S. J. & Upton, B. G. J. Two phases of sulphide saturation in Réunion magmas: evidence from cumulates. *Earth Planet. Sci. Lett.* **337–338**, 104–113 (2012).
85. Fortin, M.-A., Riddle, J., Desjardins-Langlais, Y. & Baker, D. R. The effect of water on the sulfur concentration at sulfide saturation (SCSS) in natural melts. *Geochim. et Cosmochim. Acta* **160**, 100–116 (2015).
86. Li, C. & Ripley, E. M. Empirical equations to predict the sulfur content of mafic magmas at sulfide saturation and applications to magmatic sulfide deposits. *Miner. Deposita.* **40**, 218–230 (2005).
87. O'Neill, H. S. T. C. & Mavrogenes, J. A. The sulfide capacity and the sulfur content at sulfide saturation of silicate melts at 1400 °C and 1 bar. *J. Petrol.* **43**, 1049–1087 (2002).
88. Ripley, E. M. & Li, C. Sulfide saturation in mafic magmas: is external sulfur required for magmatic Ni-Cu-(PGE) Ore Genesis? *Econ. Geol.* **108**, 45–58 (2013).
89. Hartley, M. E., Bali, E., Maclennan, J., Neave, D. A. & Halldórsson, S. A. Melt inclusion constraints on petrogenesis of the 2014–2015 Holuhraun eruption, Iceland. *Contrib. Mineral. Petrol.* **173**, 10 (2018).
90. Gudmundsson, M. T. et al. Gradual caldera collapse at Bárdarbunga volcano, Iceland, regulated by lateral magma outflow. *Science* **353**, aaf8988 (2016).
91. Bonny, E., Thordarson, T., Wright, R., Höskuldsson, A. & Jónsdóttir, I. The volume of lava erupted during the 2014 to 2015 Eruption at Holuhraun, Iceland: a comparison between satellite- and ground-based measurements. *J. Geophys. Res.: Solid Earth* **123**, 5412–5426 (2018).
92. Pfeffer, M. A. et al. Ground-based measurements of the 2014–2015 Holuhraun Volcanic Cloud (Iceland). *Geosciences* **8**, 29 (2018).
93. Carlsen, H. K. et al. Increased respiratory morbidity associated with exposure to a mature volcanic plume from a large Icelandic fissure eruption. *Nat. Commun.* **12**, 2161 (2021).
94. Carlsen, H. K. et al. Severe volcanic SO2 exposure and respiratory morbidity in the Icelandic population – a register study. *Environ. Health* **20**, 23 (2021).
95. Galeczka, I., Sigurdsson, G., Eiriksdottir, E. S., Oelkers, E. H. & Gislason, S. R. The chemical composition of rivers and snow affected by the 2014/2015 Bárðarbunga eruption, Iceland. *J. Volcano. Geotherm. Res.* **316**, 101–119 (2016).
96. Schmidt, A. et al. Satellite detection, long-range transport, and air quality impacts of volcanic sulfur dioxide from the 2014–2015 flood lava eruption at Bárðarbunga (Iceland). *J. Geophys. Res.: Atmos.* **120**, 9739–9757 (2015).
97. Twigg, M. M. et al. Impacts of the 2014–2015 Holuhraun eruption on the UK atmosphere. *Atmos. Chem. Phys.* **16**, 11415–11431 (2016).
98. Simmons, I. C. et al. Extended SO2 outgassing from the 2014–2015 Holuhraun lava flow field, Iceland. *Bull. Volcanol.* **79**, 79 (2017).
99. Bali, E., Hartley, M. E., Halldórsson, S. A., Gudfinnsson, G. H. & Jakobsson, S. Melt inclusion constraints on volatile systematics and degassing history of the 2014–2015 Holuhraun eruption, Iceland. *Contrib. Mineral. Petrol.* **173**, 9 (2018).
100. McCarthy, A. et al. Taking the pulse of volcanic eruptions using plagioclase glomerocrysts. *Earth Planet. Sci. Lett.* **552**, 116596 (2020).
101. Hartley, M. et al. The role of sulfides in controlling volcanic SO_2 emissions from Icelandic eruptions: a textural approach. (2017).
102. Leibrandt, S. & Le Pennec, J.-L. Towards fast and routine analyses of volcanic ash morphometry for eruption surveillance applications. *J. Volcanol. Geotherm. Res.* **297**, 11–27 (2015).
103. Liu, E. J., Cashman, K. V. & Rust, A. C. Optimising shape analysis to quantify volcanic ash morphology. *GeoResJ* **8**, 14–30 (2015).
104. Maclennan, J. Bubble formation and decrepitation control the CO2 content of olivine-hosted melt inclusions. *Geochem. Geophys. Geosyst.* **18**, 597–616 (2017).
105. Hartley, M. E., Shorttle, O., Maclennan, J., Moussallam, Y. & Edmonds, M. Olivine-hosted melt inclusions as an archive of redox heterogeneity in magmatic systems. *Earth Planet. Sci. Lett.* **479**, 192–205 (2017).
106. Wieser, P. & Gleeson, M. PySulfSat: An Open-Source Python3 Tool for modelling sulfide and sulfate saturation. (2023).
107. Óladóttir, B. A. Holocene eruption history and magmatic evolution of the subglacial volcanoes, Grímsvötn, Bárdarbunga and Kverkfjöll beneath Vatnajökull, Iceland. (2009).
108. Óladóttir, B. A., Sigmarsson, O., Larsen, G. & Devidal, J.-L. Provenance of basaltic tephra from Vatnajökull subglacial volcanoes, Iceland, as determined by major- and trace-element analyses. *Holocene* **21**, 1037–1048 (2011).
109. Óladóttir, B. A., Larsen, G. & Sigmarsson, O. Holocene volcanic activity at Grímsvötn, Bárdarbunga and Kverkfjöll subglacial centres beneath Vatnajökull, Iceland. *Bull. Volcanol.* **73**, 1187–1208 (2011).
110. Danyushevsky, L. V. & Plechov, P. Petrolog3: Integrated software for modeling crystallization processes. *Geochem. Geophys. Geosyst.* **12**, 1–32 (2011).
111. Langmuir, C. H., Klein, E. M. & Plank, T. Petrological Systematics of Mid-Ocean Ridge Basalts: Constraints on Melt Generation Beneath Ocean Ridges. in *Mantle Flow and Melt Generation at Mid-Ocean Ridges* 183–280 (American Geophysical Union (AGU), 1992). https://doi.org/10.1029/GM071p0183.
112. Novella, D., Maclennan, J., Shorttle, O., Prytulak, J. & Murton, B. J. A multi-proxy investigation of mantle oxygen fugacity along the Reykjanes Ridge. *Earth Planet. Sci. Lett.* **531**, 115973 (2020).

113. Schipper, C. I. & Moussallam, Y. Temporal redox variation in basaltic tephra from Surtsey volcano (Iceland). *Bull. Volcanol.* **79**, 71 (2017).
114. Nikkola, P. et al. Mid-crustal storage and crystallization of Eyjafjallajokull ankaramites, South Iceland. (2019).
115. Beattie, P., Ford, C. & Russell, D. Partition coefficients for olivine-melt and orthopyroxene-melt systems. *Contrib. Mineral. Petrol.* **109**, 212–224 (1991).
116. Mysen, B. O. Experimental determination of nickel partition coefficients between liquid, pargasite, and garnet peridotite minerals and concentration limits of behavior according to Henry's law at high pressure and temperature. *Am. J. Sci.* **278**, 217–243 (1978).
117. Bougault, H. & Hekinian, R. Rift Valley in the Atlantic Ocean near 36°50′N: petrology and geochemistry of basaltic rocks. *Earth Planet. Sci. Lett.* **24**, 249–261 (1974).
118. Greaney, A. T. et al. The behavior of chalcophile elements during magmatic differentiation as observed in Kilauea Iki lava lake, Hawaii. *Geochim. et Cosmochim. Acta* **210**, 71–96 (2017).
119. Shorttle, O. et al. Fe-XANES analyses of Reykjanes Ridge basalts: Implications for oceanic crust's role in the solid Earth oxygen cycle. *Earth Planet. Sci. Lett.* **427**, 272–285 (2015).
120. Liu, E. J., Cashman, K. V., Rust, A. C. & Edmonds, M. Insights into the dynamics of mafic magmatic-hydromagmatic eruptions from volatile degassing behaviour: the Hverfjall Fires, Iceland. *J. Volcanol. Geotherm. Res.* **358**, 228–240 (2018).
121. Jugo, P. J., Wilke, M. & Botcharnikov, R. E. Sulfur K-edge XANES analysis of natural and synthetic basaltic glasses: implications for S speciation and S content as function of oxygen fugacity. *Geochim. et Cosmochim. Acta* **74**, 5926–5938 (2010).
122. Iacovino, K. & Till, C. B. DensityX: a program for calculating the densities of magmatic liquids up to 1,627 °C and 30 kbar. *Volcanica* **2**, 1–10 (2019).
123. Keith, M., Haase, K. M., Klemd, R., Schwarz-Schampera, U. & Franke, H. Systematic variations in magmatic sulphide chemistry from mid-ocean ridges, back-arc basins and island arcs. *Chem. Geol.* **451**, 67–77 (2017).
124. Moune, S., Sigmarsson, O., Thordarson, T. & Gauthier, P.-J. Recent volatile evolution in the magmatic system of Hekla volcano, Iceland. *Earth Planet. Sci. Lett.* **255**, 373–389 (2007).
125. Shorttle, O. & Maclennan, J. Compositional trends of Icelandic basalts: implications for short–length scale lithological heterogeneity in mantle plumes. *Geochem. Geophys. Geosyst.* **12**, 1–32, (2011).
126. Wright, T. L. & Fiske, R. S. Origin of the Differentiated and Hybrid Lavas of Kilauea Volcano, Hawaii1. *J. Petrol.* **12**, 1–65 (1971).
127. Wieser, P. E. et al. Thermobar: an open-source Python3 tool for thermobarometry and hygrometry. *Volcanica* **5**, 349–384 (2022).
128. Ágústsdóttir, T. et al. Strike-slip faulting during the 2014 Bárðarbunga-Holuhraun dike intrusion, central Iceland. *Geophys. Res. Lett.* **43**, 1495–1503 (2016).
129. Caracciolo, A. et al. Temporal evolution of magma and crystal mush storage conditions in the Bárðarbunga-Veiðivötn volcanic system, Iceland. *Lithos* **352–353**, 105234 (2020).
130. Neave, D. A., Passmore, E., Maclennan, J., Fitton, G. & Thordarson, T. Crystal–melt relationships and the record of deep mixing and crystallization in the ad 1783 Laki Eruption, Iceland. *J. Petrol.* **54**, 1661–1690 (2013).
131. Cashman, K. V. Crystal Size Distribution (CSD) analysis of volcanic samples: advances and challenges. *Front. Earth Sci.* **8**, 1–17 (2020).
132. Cashman, K. V. & Marsh, B. D. Crystal size distribution (CSD) in rocks and the kinetics and dynamics of crystallization II: Makaopuhi lava lake. *Contr. Mineral. Petrol.* **99**, 292–305 (1988).
133. Edmonds, M. RESEARCH FOCUS: flotation of magmatic minerals. *Geology* **43**, 655–656 (2015).
134. Gualda, G. A. R. & Ghiorso, M. S. Magnetite scavenging and the buoyancy of bubbles in magmas. Part 2: Energetics of crystal-bubble attachment in magmas. *Contrib. Mineral. Petrol.* **154**, 479–490 (2007).
135. Knipping, J. L., Webster, J. D., Simon, A. C. & Holtz, F. Accumulation of magnetite by flotation on bubbles during decompression of silicate magma. *Sci. Rep.* **9**, 3852 (2019).
136. Mungall, J. E. & Su, S. Interfacial tension between magmatic sulfide and silicate liquids: Constraints on kinetics of sulfide liquation and sulfide migration through silicate rocks. *Earth Planet. Sci. Lett.* **234**, 135–149 (2005).
137. Yao, Z. & Mungall, J. E. Flotation mechanism of sulphide melt on vapour bubbles in partially molten magmatic systems. *Earth Planet. Sci. Lett.* **542**, 116298 (2020).
138. Moussallam, Y. et al. The impact of degassing on the oxidation state of basaltic magmas: A case study of Kīlauea volcano. *Earth Planet. Sci. Lett.* **450**, 317–325 (2016).
139. Pedersen, G. B. M. et al. Lava field evolution and emplacement dynamics of the 2014–2015 basaltic fissure eruption at Holuhraun, Iceland. *J. Volcanol. Geotherm. Res.* **340**, 155–169 (2017).
140. Zhang, Y., Xu, Z., Zhu, M. & Wang, H. Silicate melt properties and volcanic eruptions. *Rev. Geophys.* **45**, 1–27 (2007).
141. Freda, C., Baker, D. R. & Scarlato, P. Sulfur diffusion in basaltic melts. *Geochim. et Cosmochim. Acta* **69**, 5061–5069 (2005).
142. Ding, S., Plank, T., Wallace, P. J. & Rasmussen, D. J. Sulfur_X: a model of sulfur degassing during magma ascent. *Geochem. Geophys. Geosyst.* **24**, e2022GC010552 (2023).
143. Mastin, L. G. Evidence for water influx from a caldera lake during the explosive hydromagmatic eruption of 1790, Kilauea volcano, Hawaii. *J. Geophys. Res.: Solid Earth* **102**, 20093–20109 (1997).
144. Mastin, L. G., Christiansen, R. L., Thornber, C., Lowenstern, J. & Beeson, M. What makes hydromagmatic eruptions violent? Some insights from the Keanakāko'i Ash, Kīlauea Volcano, Hawai'i. *J. Volcanol. Geotherm. Res.* **137**, 15–31 (2004).
145. Zelenski, M., Simakin, A., Taran, Y., Kamenetsky, V. S. & Malik, N. Partitioning of elements between high-temperature, low-density aqueous fluid and silicate melt as derived from volcanic gas geochemistry. *Geochim. et Cosmochim. Acta* **295**, 112–134 (2021).
146. Guo, H. & Audétat, A. Transfer of volatiles and metals from mafic to felsic magmas in composite magma chambers: an experimental study. *Geochim. et Cosmochim. Acta* **198**, 360–378 (2017).
147. Zajacz, Z., Halter, W. E., Pettke, T. & Guillong, M. Determination of fluid/melt partition coefficients by LA-ICPMS analysis of co-existing fluid and silicate melt inclusions: controls on element partitioning. *Geochim. et Cosmochim. Acta* **72**, 2169–2197 (2008).
148. Candela, P. A. & Holland, H. D. A mass transfer model for copper and molybdenum in magmatic hydrothermal systems; the origin of porphyry-type ore deposits. *Econ. Geol.* **81**, 1–19 (1986).
149. Keppler, H. & Wyllie, P. J. Partitioning of Cu, Sn, Mo, W, U, and Th between melt and aqueous fluid in the systems haplogranite-H2O−HCl and haplogranite-H2O−HF. *Contr. Mineral. Petrol.* **109**, 139–150 (1991).
150. Williams, T. J., Candela, P. A. & Piccoli, P. M. The partitioning of copper between silicate melts and two-phase aqueous fluids: an experimental investigation at 1 kbar, 800° C and 0.5 kbar, 850 °C. *Contrib. Mineral. Petrol.* **121**, 388–399 (1995).
151. Sigvaldason, G. E. & Óskarsson, N. Chlorine in basalts from Iceland. *Geochim. et Cosmochim. Acta* **40**, 777–789 (1976).
152. Aiuppa, A. Degassing of halogens from basaltic volcanism: insights from volcanic gas observations. *Chem. Geol.* **263**, 99–109 (2009).
153. Mason, E. M. et al. Chalcophile element processing at an active continental arc volcano. *Geochim. et Cosmochim. Acta* S0016703723006348 https://doi.org/10.1016/j.gca.2023.12.014 (2023).
154. Beaudry, P. et al. Degassing-induced fractionation of multiple sulphur isotopes unveils post-Archaean recycled oceanic crust signal in hotspot lava. *Nat. Commun.* **9**, 5093 (2018).

155. Cabral, R. A. et al. Anomalous sulphur isotopes in plume lavas reveal deep mantle storage of Archaean crust. *Nature* **496**, 490–493 (2013).
156. Desborough, G. A., Anderson, A. T. & Wright, T. L. Mineralogy of sulfides from certain Hawaiian basalts. *Econ. Geol.* **63**, 636–644 (1968).
157. Helz, R. T., Cottrell, E., Brounce, M. N. & Kelley, K. A. Olivine-melt relationships and syneruptive redox variations in the 1959 eruption of Kīlauea Volcano as revealed by XANES. *J. Volcanol. Geotherm. Res.* **333–334**, 1–14 (2017).
158. Helz, R. T. & Wright, T. L. Differentiation and magma mixing on Kilauea's east rift zone. *Bull. Volcanol.* **54**, 361–384 (1992).
159. Moore, R. B. et al. The 1977 eruption of Kilauea volcano, Hawaii. *J. Volcanol. Geotherm. Res.* **7**, 189–210 (1980).
160. Yoshimura, S. Diffusive fractionation of H2O and CO2 during magma degassing. *Chem. Geol.* **411**, 172–181 (2015).
161. Johnson, A. & Canil, D. The degassing behavior of Au, Tl, As, Pb, Re, Cd and Bi from silicate liquids: experiments and applications. *Geochim. et Cosmochim. Acta* **75**, 1773–1784 (2011).
162. MacKenzie, J. M. & Canil, D. Volatile heavy metal mobility in silicate liquids: implications for volcanic degassing and eruption prediction. *Earth Planet. Sci. Lett.* **269**, 488–496 (2008).
163. Mangan, M. T. & Cashman, K. V. The structure of basaltic scoria and reticulite and inferences for vesiculation, foam formation, and fragmentation in lava fountains. *J. Volcano. Geotherm. Res.* **73**, 1–18 (1996).
164. Stovall, W. K., Houghton, B. F., Hammer, J. E., Fagents, S. A. & Swanson, D. A. Vesiculation of high fountaining Hawaiian eruptions: episodes 15 and 16 of 1959 Kīlauea Iki. *Bull. Volcanol.* **74**, 441–455 (2012).
165. Swanson, D. A. & Fabbi, B. P. Loss of volatiles during fountaining and flowage of basaltic lava at Kilauea Volcano, Hawaii. *J. Res. US Geol. Surv.* **1**, 649–658 (1973).
166. Liotta, M. et al. Mobility of plume-derived volcanogenic elements in meteoric water at Nyiragongo volcano (Congo) inferred from the chemical composition of single rainfall events. *Geochim. et Cosmochim. Acta* **217**, 254–272 (2017).
167. Stewart, C. et al. Volcanic air pollution and human health: recent advances and future directions. *Bull. Volcanol.* **84**, 11 (2021).
168. Rueden, C. T. et al. ImageJ2: ImageJ for the next generation of scientific image data. *BMC Bioinform.* **18**, 529 (2017).
169. Higgins, M. D. Measurement of crystal size distributions. *Am. Mineral.* **85**, 1105–1116 (2000).
170. Jenner, F. E. & O'Neill, H. St. C. Analysis of 60 elements in 616 ocean floor basaltic glasses: TECHNICAL BRIEF. *Geochem. Geophys. Geosyst.* **13**, n/a–n/a (2012).
171. Roeder, P. L. & Emslie, R. F. Olivine-liquid equilibrium. *Contr. Mineral. Petrol.* **29**, 275–289 (1970).
172. Matzen, A. K., Baker, M. B., Beckett, J. R. & Stolper, E. M. Fe–Mg partitioning between olivine and high-magnesian melts and the nature of hawaiian parental liquids. *J. Petrol.* **52**, 1243–1263 (2011).
173. Toplis, M. J. The thermodynamics of iron and magnesium partitioning between olivine and liquid: criteria for assessing and predicting equilibrium in natural and experimental systems. *Contrib. Mineral. Petrol.* **149**, 22–39 (2005).
174. Putirka, K. D. Thermometers and barometers for volcanic systems. *Rev. Mineral. Geochem.* **69**, 61–120 (2008).
175. Namur, O. et al. Anorthosite formation by plagioclase flotation in ferrobasalt and implications for the lunar crust. *Geochim. et Cosmochim. Acta* **75**, 4998–5018 (2011).
176. Putirka, K. D. Igneous thermometers and barometers based on plagioclase + liquid equilibria: tests of some existing models and new calibrations. *Am. Mineral.* **90**, 336–346 (2005).

Acknowledgements

The authors acknowledge support from a NERC urgency grant NE/M021130/1 'Source and longevity of sulphur in Icelandic flood basalt eruption plumes' to E.I., M.E., M.E.H. and T.T. F.E.J. and B.E.K. acknowledge funding from NERC grant 'From Arc Magmas to Ores (FAMOS): A mineral Systems Approach'(NE/P017045/1). EJN acknowledges an Early Career Fellowship from the Leverhulme Trust. PW acknowledges startup funds from UC Berkeley. The samples used in this study were collected by the Holuhraun Eruption Team, with the exception of sample E.I. collected by E.I. and colleagues as part of the urgency grant. The authors thank Tamsin Mather for insightful discussion, and Shuo Ding for help running SulfurX models.

Author contributions

EJN, ME and EI conceived the project. MH, TT and EI collected samples. EJN performed textural and geochemical measurements and led the initial manuscript draft, data interpretation and discussion, and first response to reviewers. PW performed fractional crystallization calculations, SCSS and S degassing models and mineral equilibrium calculations, writing the associated text sections. She also coordinated the final set of revisions and proofs. FJ and BK helped with LA-ICPMS analyses. All authors contributed to the writing and editing of the manuscript.

Competing interests

E.L. is an Editorial Board Member for Communications Earth & Environment, but was not involved in the editorial review of, nor the decision to publish this article. Other than this, the authors declare no competing interests.

Additional information

Supplementary information The online version contains supplementary material available at https://doi.org/10.1038/s43247-024-01249-2.

Correspondence and requests for materials should be addressed to Emma J. Nicholson, Penny E. Wieser or Marie Edmonds.

Peer review information *Communications Earth & Environment* thanks Allan Lerner, Bertrand Rottier and the other, anonymous, reviewer(s) for their contribution to the peer review of this work. Primary Handling Editor: Joe Aslin.